Hunter, Stuart Michael (2008) *A structural and reactivity study of lithium molybdenum nitride.* MSc(R) thesis.

http://theses.gla.ac.uk/93/

A Structural and Reactivity study of Lithium Molybdenum Nitride

Stuart Michael Hunter BSc (Hons.)

UNIVERSITY
of
GLASGOW

Thesis submitted to the University of Glasgow for the degree of

Master of Science

Department of Chemistry

Declaration

The work contained in this thesis, submitted for the degree of MSc, its own original work, except where due reference is made to other authors. No material within has been previously submitted for a degree at this or any other institution.

\-

Stuart Michael Hunter

Abstract

This thesis describes the preparation and reactivity of lithium molybdenum nitride samples and the preparation and characterisation of the nitride precursors. It has been shown that samples containing lithium molybdenum nitride ($LiMoN_2$) can be formed from the direct ammonolysis of lithium molybdate (Li_2MoO_4), although it has proved challenging to produce the nitride as a single phase material.

The "$LiMoN_2$" samples were observed to be catalytically active for ammonia synthesis in reaction with nitrogen containing feed gas (25% N_2/H_2). An impurity, which cannot be indentified through powder X-ray diffraction, was demonstrated to be the likely active phase in the sample.

The role of 'lattice' nitrogen in the ammonia synthesis reaction was investigated through reactions with a feed gas with no source of nitrogen present (25% Ar/H_2). It was shown that this proposed active phase will produce ammonia, in the absence of nitrogen in the feed gas.

One candidate impurity that could be responsible for this anomalous activity was lithium nitride. Reactions were conducted and it was seen that lithium nitride was very active in the production of ammonia. Subsequent investigations showed that the generation of ammonia probably originates from the direct decomposition of lithium amide.

Contents

List of Figures

List of Tables

1 Introduction

1.1 Background

1.1.1 Nitrides

The significant and rapid progress in nitride chemistry has been seen over the last decade or so with improved classification and development of new synthetic routes leading to new nitride materials. The synthesis of nitrides is still very complex with large thermodynamic barriers which occur from the making and breaking of N≡N bonds (945 kJmol^{-1} for N≡N compared to 498 kJmol^{-1} for O=O). Many nitrides, especially those containing s-block elements, are air and moisture sensitive, and rapidly form oxides, hydroxides and ammonia upon contact with oxygen or moisture. These factors can therefore contribute to the low abundance of nitride compounds, compared to those of the oxides or carbides[1].

Recent developments in the handling methods for air sensitive samples and improved diffraction techniques have led to a revival in the area of nitride chemistry and thus a large increase in research.

There are many sub-groups of nitrides from binary and ternary nitrides[2] to oxynitrides and nitride halides. Nitrides can be sub-divided into ionic, covalent and interstitial types[1].

The progress from binary to higher nitrides was initially hampered by issues with synthetic procedures and the analytical methods used. This however has meant that there are numerous binary nitrides of metals and non-metals that are well characterised. Many have very useful applications such as semiconductors (GaN), optoelectronic devices (AlN, GaN and InN)[3] and high temperature refractory ceramics (AlN, BN and TiN)[1].

Alkali metal nitrides are dominated by lithium nitride, Li_3N. There are wide ranging methods of producing Li_3N, from the reaction of nitrogen with lithium dissolved in liquid sodium[4] to the high temperature reaction of solid lithium under nitrogen. Originally lithium nitride had been proposed to have a cubic molecular lattice[5], however it was correctly characterised structurally in the 1930s by Zintl

and Brauer[6]. The structure that they proposed was one of a nitrogen atom surrounded by eight lithium atoms, six lithium atoms in the same plane, trigonally coordinated to the nitrogen atom, and one linearly coordinated to the nitrogen atom above and below the plane, thus forming a hexagonal bipyramid (Figure 1-1). In 1976, Rabenau and Schulz determined the space group was P6/mmm[7].
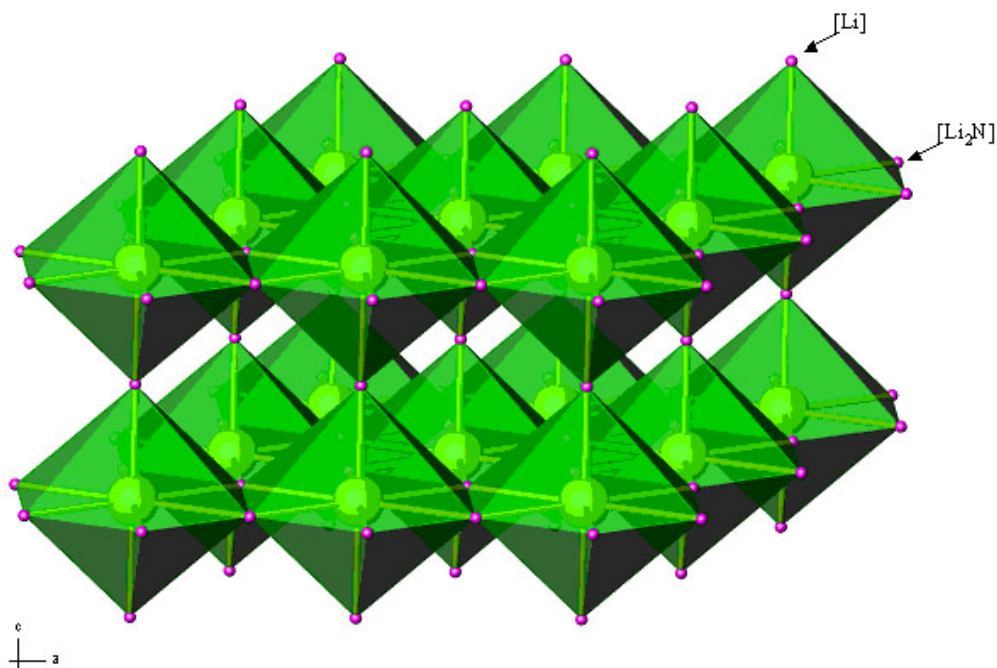
Figure 1-1: Structure of Lithium Nitride.
Purple spheres – Li, Green Spheres – N, hexagonal bipryamidal structure space group P6/mmc.

Boukamp and Huggins showed that polycrystalline Li_3N had a Li-ion conductivity of approx. $10^{-4}\Omega^{-1}cm^{-1}$ [8]. Recent work has been done looking at lithium nitridometalates $Li_{3-x-y}M_xN$ (M = Cu, Co, Ni; y = Li vacancy). These have been shown to be promising for anode materials. The substitution of the transition metal has important consequences for the physical properties[9,10] and it has been shown that substitution of an aliovalent transition metal increases the conductivity in the nitride[11].

Ionic conductivity is reported to occur due to a vacancy hopping mechanism and when taking into consideration that the Li^+ ions which are in the same plane as the nitrogen ion are more weakly bound than those above and below the plane, it was concluded that the mechanism occurs between lithium ions in the $[Li_2N]$ plane perpendicular to the c-axis. There are two separate mechanisms operating within lithium nitride. The above mechanism is found to be in operation at temperatures

below 300K, but upon increasing the temperature, a second process, in which the conduction was occurring parallel to the c-axis, begins to take place.

The potential applications that have been looked at for lithium nitride include hydrogen storage for use in hydrogen-oxygen fuel cells; this has arisen in the search for cleaner energy as a means to replace fossil fuels. Application as a solid electrolyte in lithium ion batteries has also been investigated.

The existence of heavier alkali metal nitrides is debateable due to their low thermodynamic stability. Recent work has been conducted into sodium nitride [12,13,14] and potassium nitride[15]. Sodium nitride has been synthesised via the deposition of the desired elements as an atomic level dispersion and, the resulting solid formed at liquid nitrogen temperatures, ordered structures are formed on heating[12]. However more recently the plasma assisted synthesis[13] has been described by Vajenine, in which elemental sodium with gaseous nitrogen is activated by capacitive high frequency discharge at pressures of up to 4 mbar without heating.

Alkaline earth nitrides have also been synthesised by reactions involving non-gaseous sources of nitrogen, e.g. decomposition of sodium azide[16,17]. Sodium flux reactions also take advantage of this decomposition, from which the sodium is derived. This method has been shown to be a superior way of producing single crystals of a good enough quality for single crystal X-ray diffraction analysis. NaN_3 decomposition reactions generate high pressures when the metal and gaseous N_2 form, thus autoclaves or sealed vessels are used.

More reactive gaseous nitrogen sources, such as ammonia or mixtures of hydrogen and nitrogen, have been used in reactions with oxide, halide or sulfide precursors to form both binary and ternary transition metal nitrides. These have been reported to be successful at much lower temperatures than the more traditional solid state synthesis methods[18,19,20]. This is limited to a very specific temperature range outside of which an incomplete reaction, a partially crystalline product, or thermal decomposition is observed. Oxynitrides especially can be very difficult to distinguish from nitride products, leading to the theory that many nitrides assigned in the literature are possibly imides, amides and oxynitrides[21].

Ternary nitrides were investigated initially by Juza *et al.*[2] from the 1940s onwards. The initial synthesis methods for formation of ternary nitrides containing lithium were; (1) nitriding of a mixture of $Li_3N + M$ with N_2 or NH_3; (2) nitriding of an alloy Li_mM and (3) reaction of binary nitrides ($Li_3N + M_nN$) under a N_2 atmosphere. Further methods have been used to synthesise nitrides including the production of Ni-Mo bimetallic nitrides[22] via the programmed temperature reaction of the bimetallic oxide with a mixture of H_2 and N_2 gas instead of NH_3. The formation of the nitrides is also possible from a reaction in a salt melt or through preparation from other ternary nitrides, or through reactions in autoclaves[23].

The early 1990s saw a rapid increase in the number of alkaline- and alkaline earth-metal-transition-metal nitrides including MNiN (M = Ca, Sr or Ba)[24], Ba_3MN_4 (M = Mo and W) and $M_2LiFe_2N_3$ (M = Sr and Ba). The potential applications for ternary nitrides are wide ranging from novel semiconductors and superconductors to corrosion resistant materials; these are being used to enhance processes and products. Titanium aluminium nitride (TiAlN) is being used as a wear-, corrosion-, and diffusion-resistant coating for cutting and drilling tools. The creation of improved diffusion barriers has enabled the use of copper interconnects in integrated circuits allowing advances in a new generation of faster computer chips[25]. Other research shows how they have applications such as high temperature ceramics[26], catalysts or magnetic materials[19].

The formation of the transition metal nitrides is possible via a wide variety of methods from the conventional high temperature processes to the moderate-temperature conditions seen in topotactic transformations and the novel uses of sulfides and nitridation precursors[27].

Many ternary and higher nitride structures that have been formed contain transition metals that display very unusual co-ordination to nitrogen. Ternary nitrides that display this are A_3MN_3 (A = alkaline earth, M = V, Cr, Mn, Fe)[28,29] and Ca_6MN_5 (M = Fe, Ga, Mn)[30] which contain M^{3+} co-ordinated to three nitrogen atoms.

Ternary nitrides of the stoichiometry AMN_2 (A = alkali metal, alkaline earth metal or transition metal; M = transition metal or lanthanide) crystallize into a variety of different structures. For example, $LiMN_2$ (M = Mo or W) are hexagonally coordinated to six nitrogen atoms in a trigonal prismatic coordination[18,31] ($LiMoN_2$ is explored in further detail in section 1.1.4). In $NaMN_2$ (M = Nb, Ta) the cations are coordinated to nitrogen in an octahedral geometry[32,33].

Bimetallic molybdenum nitrides have been synthesised and used in hydrogenation reactions, for example the Fischer-Tropsch reaction[34,35], hydrodenitrogenation (HDN) and hydrodesufurization (HDS)[36,37].

1.1.2   Catalysis

In general terms, catalysis is an acceleration of the rate of a process or reaction, brought about by a separate compound, usually present in small and managed quantities. It permits reactions or processes to take place more effectively or under milder conditions than would otherwise be possible.

The term 'catalysis' was first coined in 1835 when the chemist J. J. Berzelius proposed that a catalyst is a compound which, when added to a chemical reaction, increases the rate of the reaction but the compound itself is not consumed in the reaction. Therefore the catalyst, for heterogeneous systems, more often than not acts as a place for a reaction to occur with some reactants adsorbed onto the surface. Additional reactants react with the molecules adsorbed on the surface and the products are then desorbed from the catalyst leaving the active site free for further reactions to take place.

Heterogeneous catalysis is where the catalyst and the reactants are in different phases, e.g. a solid catalyst with a gas phase reactant. It is widely used in industry due to its robustness, ease of separation of the catalyst from the products formed and its relative cheapness in comparison to homogeneous catalysts. An example of heterogeneous catalysis is in catalytic converters on cars to eliminate carbon and nitrogen monoxides from the exhaust gases. The surface of the catalyst acts as a site for carbon and nitrogen monoxides to adsorb onto, they then react and desorbs as carbon dioxide and nitrogen gas.

$$2CO_{(g)} + 2NO_{(g)} \xrightarrow{\text{Pt/Pd/Rh}} 2CO_{2(g)} + N_{2(g)}$$
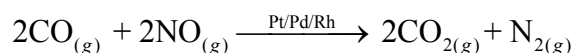
1.1.3   Ammonia Synthesis Catalysts

The search for catalysts to be used in the synthesis of ammonia has been pursued for the last 90 years. In 2005 the worldwide production of ammonia totalled 121 million tonnes[38] with 80% of this being used for fertilisers. New catalysts are being sought in order to allow for the current Haber process (iron catalyst) which uses high pressures (~250atm) and temperatures (400-500°C) to be surpassed by a reaction which requires less harsh conditions. Schlögl in his review[39] looks at the progress of new ammonia synthesis catalysts which are being seen as a possible replacement of the current iron catalyst.

One possibility for this would be molybdenum nitride, which has been well established[40,41,42,43]. The rate determining step was originally thought (according to Hillis *et al.*[40]) to be the conversion of adsorbed nitrogen to gas phase NH_3 rather than the actual nitrogen adsorption. Subsequently this was investigated by Aika and Ozaki[41] who argued that the adsorption of nitrogen was the rate determining step. With various molybdenum nitride structures possible the surface area and activity of the catalyst is variable. It is therefore possible to produce high and low surface area catalysts of γ-Mo_2N. This means that the synthetic route to the nitride will have a large effect on the catalytic activity of the catalyst[44]. The system however shows signs of ammonia decomposition which is detrimental to an ammonia synthesis catalyst.

Recent research has shown that Cs^+ doped ternary molybdenum nitride (Co_3Mo_3N) has a higher activity than the commercial iron catalyst. Applying the volcano principle, in which components possessing both weak and strong nitrogen binding strengths are combined to form a catalyst with optimal binding strength, Jacobsen *et al.*[45] rationalised the high activity of Co_3Mo_3N. Structural nitrogen is proposed to be a requirement due to its ability to stabilise the active (111) surface plane.

It has been shown in recent work that the η-6 Co_3Mo_3N has interesting properties and under harsh reduction conditions with 25% Ar/H_2 is transformed to η-12

Co_6Mo_6N. This allows for the possibility of 'lattice' nitrogen being used in a novel nitrogen transfer pathway[46].

Cs^+ Doped Co_3Mo_3N has a remarkably high activity for ammonia synthesis[47], as shown in Table 1-1. It has been shown that Cs^+-promoted catalyst at 400°C under 3.1MPa reaches 40% of the equilibrium yield, and is four times more active than the doubly promoted iron catalyst.

Table 1-1: Ammonia synthesis activities of various catalysts[48].

Catalyst	Rate ($\mu mol.hr^{-1}g^{-1}$)	Surface Area (m^2g^{-1})	Specific Activity ($\mu mol.hr^{-1}m^{-2}$)
$Fe-K_2O-Al_2O_3$	330	14	24
Co_3Mo_3N	652	21	31
Co_3Mo_3N-K (5 mol %)	869	17	51
Co_3Mo_3N-K (30 mol %)	364	8	46
Co_3Mo_3N-Cs (2 mol %)	986	16	62
Co_3Mo_3N-Cs (10 mol %)	586	10	59

The high activity of nitrides for ammonia synthesis is notable, and it is possible to question the role of 'lattice' nitrogen in the reactions of nitrides. One possibility, which has analogies in the Mars van-Krevelen mechanism[49] in oxidation catalysis with oxides, is that the 'lattice' nitrogen is itself active. This possibility has not received much attention as nitrides are perceived to be inert. Some work has been carried out using vanadium aluminium oxynitrides (VAlONs) in propane ammoxidation[50] in which a double Mars van-Krevelen redox mechanism is proposed involving 'lattice' oxygen and surface N species.

In view of the results of recent work into the activity of 'lattice' nitrogen in Mo_2N and Co_3Mo_3N, it was decided to extend studies to additional ternary molybdenum nitride systems. In this project, lithium molybdenum nitride has been investigated in this respect.

1.1.4 Lithium Molybdenum Nitride

Lithium molybdenum nitride ($LiMoN_2$) is a fairly recent discovery – DiSalvo et al.[18] reported its existence in the early 1990s. The discovery was made during their search for ternary or higher nitrides that exhibit high-T_c superconductivity similar to those of the oxides, other uses are in the area of lithium ion batteries.

Lithium molybdenum nitride can be synthesised via numerous methods such as the decomposition of $Li_2Mo(N^tBu)$ under flowing ammonia, or reaction of Li_2MoO_4 with ammonia gas. The reaction is extremely sensitive to temperature and time with the ternary nitride forming only within a very narrow temperature region. Incomplete reaction occurs at low temperatures whereas at higher temperatures partial decomposition to γ-Mo_2N is observed.

Figure 1-2: Structure of Lithium Molybdenum Nitride.
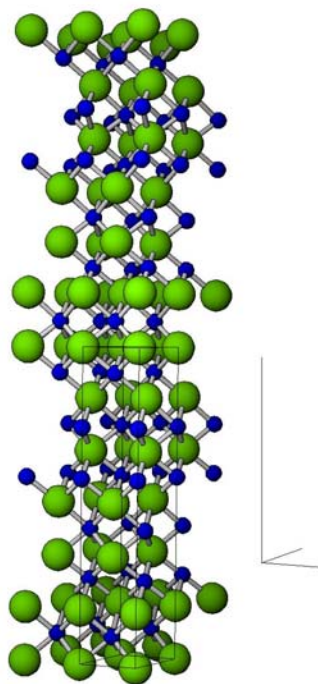
(Blue = N, Green = Li and Mo – shared site) Space group R3m.

This was the first layered metallic nitride, and the structure allows for lithium to be deintercalated and reintercalated, the structure of which is shown in Figure 1-2. It was also the first example of a ternary nitride formed from the ammonolysis of a molecular organometallic molecule ($Li_2Mo(N^tBu)_4$) or of a ternary oxide (Li_2MoO_4).

1.2 Aim

This project was designed to study the preparation and reactivity of lithium molybdenum nitride as an ammonia synthesis catalyst with a possible source of active 'lattice' nitrogen. The activity of the nitride towards ammonia synthesis in the absence of gas-phase N_2 was investigated as an example of nitrogen transfer reaction. Also investigations into the preparation and characterisation of the nitride precursor were under taken.

2 Experimental and Methodology

2.1 Sample Preparation

The sample preparation followed methods based on the literature. The nitrides were prepared in two stages, firstly synthesising a precursor and then using ammonolysis to convert the precursor into the final nitride.

The precursor, lithium molybdate, was prepared via three methods: (1) high temperature synthesis from lithium carbonate and molybdenum trioxide[18], (2) room temperature preparation using molybdenum trioxide and hydrated lithium hydroxide[51] and (3) lithium hydroxide and ammonium molybdate salt in a precipitation reaction in ethanol[52].

The precursors (from all of the above mentioned methods) were heated in a tube furnace to 710°C for 14 hours under flowing ammonia gas ($10 mlmin^{-1}$) and then cooled to room temperature, still under a flow of ammonia gas (Figure 2-1).
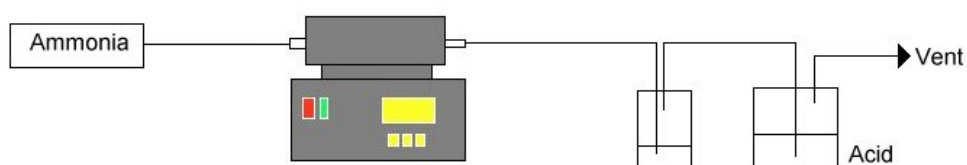
Figure 2-1: Ammonolysis Rig.
Ammonia flowed at $10 mlmin^{-1}$ over a sample situated centrally within the furnace.

2.2 Sample Testing

Materials were tested for their performance as ammonia synthesis catalysts by using a fixed bed, continuous flow, 10.5mm i.d. quartz glass reactor. 0.4g of sample in a powder form was held centrally (using silica wool plugs) within the reactor tube which was housed within a furnace.

The feed gas mixture was introduced into the reactor at a total flow rate of $60 mlmin^{-1}$, through a mass flow controller. The exhaust gas was bubbled through a dilute sulfuric acid mixture. Once the reaction was started, the conductivity change of a known concentration and volume of acid solution was used to determine the quantity of ammonia produced.

Catalyst testing was conducted under two different feed gas regimes, (a) BOC 25% nitrogen/hydrogen (stoichiometric NH_3 synthesis mixture) [25% N_2/H_2] and (b) BOC 25% argon/hydrogen [25% Ar/H_2].

The sample was first exposed for two hours at 700°C to the 25% N_2/H_2 gas mix to nitride *in-situ* to allow sufficient time for the surface of the sample to be re-nitrided before the ammonia synthesis experiments were carried out. After 2 hours at 700°C the temperature was reduced to 400°C. The exhaust gas from the reactor was then bubbled through a sulfuric acid solution, (200ml, 0.00108mol.l^{-1} and at ambient temperature) and the ammonia yield was calculated by detecting the conductivity decrease of the sulfuric acid solution with respect to time.

Each sample was tested under both feed gases. The reaction with 25% N_2/H_2 mixture was conducted for 5½ hours at 400°C. For the 25% Ar/H_2 gas the feed gas was changed after the renitriding stage and then measurements were taken when the feed gas had been changed to the Ar/H_2, during the reaction the temperature was raised by 100°C at intervals to 500°C, 600°C and finally to 700°C to see the effect on the nitrogen in the sample. The reactor set-up is shown in Figure 2-2.
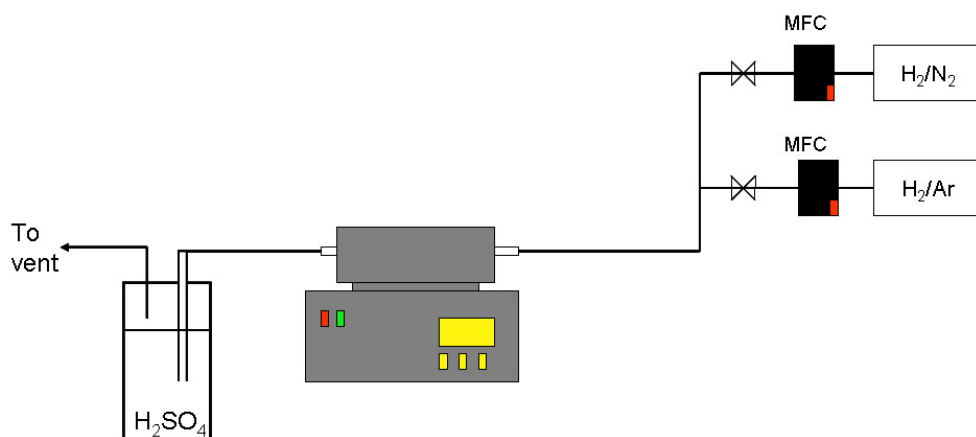
Figure 2-2: Reaction Rig.
Schematic showing the reactor setup for ammonia synthesis testing.

2.3 Characterisation

2.3.1 X-ray Diffraction

During this project, powder X-ray diffraction (XRD) was used as the main method of characterisation. This technique can be used to identify known phases rapidly and estimate sample purity. Further, by the process of indexing diffraction data unit cell parameters for samples can be determined and refined. The crystal structures can be refined by using the Rietveld method.

Bragg devised a method of explaining X-ray diffraction, where a crystal is regarded as a layered construct which gives a regularly repeating structure. Diffraction occurs when the distance between the layers (planes) are of a similar scale to that of the wavelength (λ) of the X-ray radiation and thus acts as a diffraction grating.

X-rays are generated by accelerating electrons from a tungsten filament towards a target (most commonly used examples are Cu or Mo) applying a high voltage, giving K_α wavelengths of 1.5148Å and 0.7107Å respectively. Electrons with enough energy eject core electrons from their atomic orbital causing electrons in higher energy orbitals to decay, emitting X-ray radiation (Figure 2-3Figure 2-4). The K_α X-ray wavelength is selected by using a secondary monochromator.
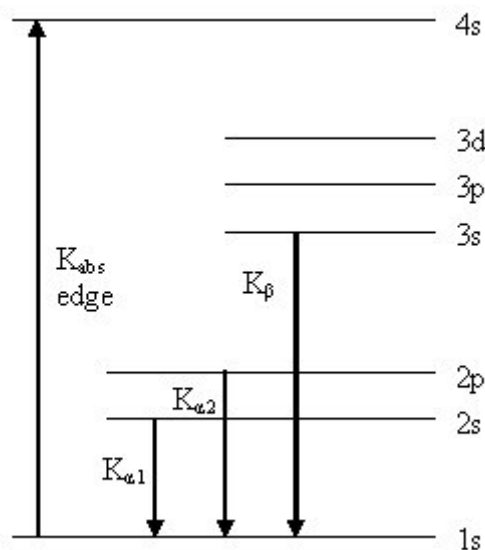
Figure 2-3: Emission Lines.
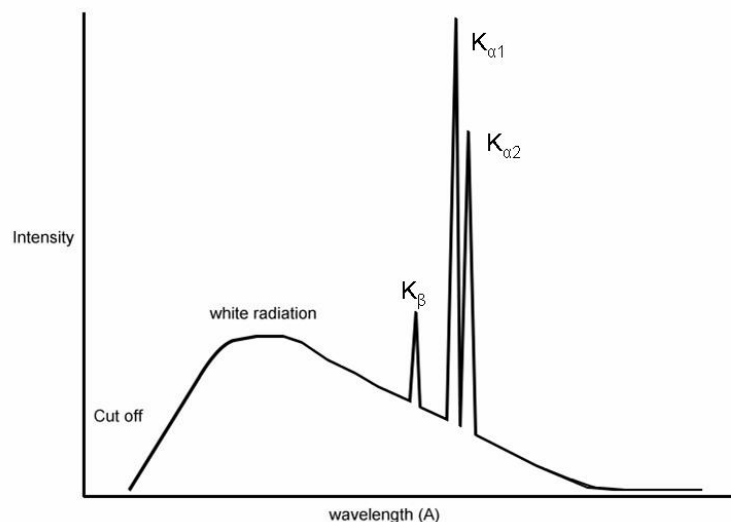
Figure 2-4: Copper emission diagram.

In a diffractometer, the X-ray beam is focused on to the sample, leading to X-ray scattering with a characteristic pattern of spots. The scattering of X-ray radiation on interaction with the electrons in a structure is described by Bragg's law (Figure 2-5) where the diffracted beams are equated to reflections from planes passing through points in the crystal.

An X-ray diffraction pattern is obtained from the elastic scattering of the X-rays by the electrons within the sample. Heavier elements have a greater number of electrons and will therefore scatter more X-rays and this increases the intensity of the observed peaks. Lighter elements (especially hydrogen) have very few electrons and as such do not scatter the X-rays as well. Liquids, glasses and amorphous solid compounds lack long range order, as such they do not produce characteristically defined diffraction patterns and thus cannot be characterised.
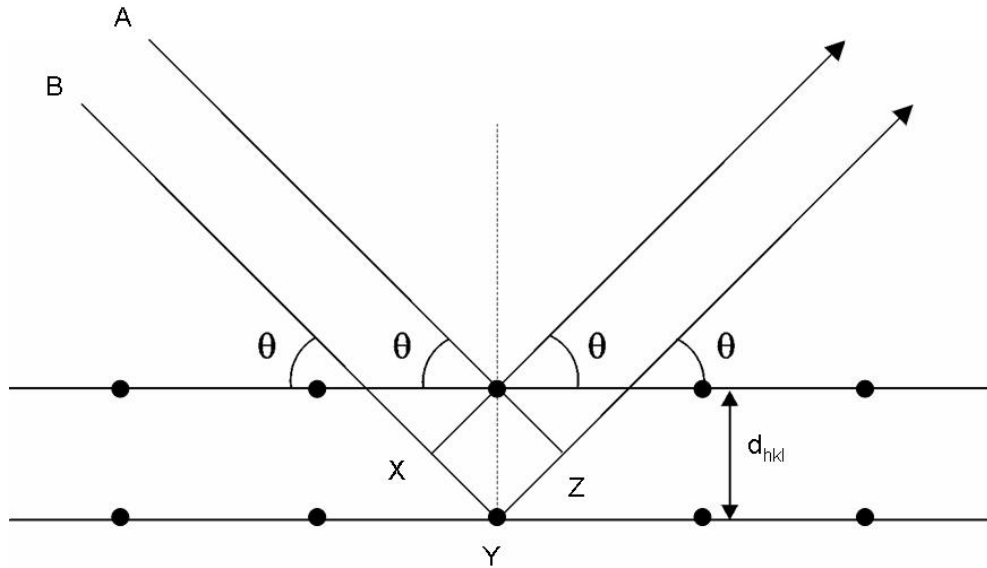
Figure 2-5: Bragg's Law Diagram.

Two parallel incident X-ray beams, A and B, must be in phase to produce constructive interference for a reflection to be produced. Beam B must travel an extra distance, XYZ, compared to beam A for the beams to remain in phase. This distance is related to the interplanar spacing d_{hkl} and angle of incidence by:

$$XYZ = 2d \sin \theta$$

Equation 1:
Where d = plane separation, θ = Bragg angle and XYZ is the path difference.

For constructive interference to occur and produce a reflection XYZ must be equal to a whole number of wavelengths:

$$XYZ = n\lambda$$

Equation 2:
Where n = an integer and λ = radiation wavelength.

Bragg's law can be achieved through a combination of equations Equation 1: and Equation:

$$n\lambda = 2d \sin \theta$$

Equation 3:
Where n is an integer, λ is the wavelength of the incident X-rays, d is the distance between the planes in the crystal and θ is the angle of incidence of the X-rays.

Crystal systems are derived from the d-values through identification of the planes involved. Planes are defined by the Miller indices, *hkl*, the reciprocal positions where the planes cut the *a*, *b* and *c* axes respectively. If, for example, the plane intersects axes at x = ½, y = ⅓ and z = ∞, the Miller index of the plane is $h = 2$, $k = 3$, $l = 0$ or (230). The values are either positive, negative or zero and useful in explaining the plane separation of a crystal. Each crystal system (cubic, tetragonal, etc) has an expression that denotes the plane separation (d_{hkl}), these are shown in Table 2-1.

Table 2-1: Equations for d-spacings in the different crystal systems.

Crystal System	Expression for d_{hkl}
Cubic	$$\frac{1}{d_{hkl}^2} = \frac{h^2 + k^2 + l^2}{a^2}$$
Tetragonal	$$\frac{1}{d_{hkl}^2} = \frac{h^2 + k^2}{a^2} + \frac{l^2}{c^2}$$
Orthorhombic	$$\frac{1}{d_{hkl}^2} = \frac{h^2}{a^2} + \frac{k^2}{b^2} + \frac{l^2}{c^2}$$
Hexagonal	$$\frac{1}{d_{hkl}^2} = \frac{4}{3}\left(\frac{h^2 + hk + k^2}{a^2}\right) + \frac{l^2}{c^2}$$
Monoclinic	$$\frac{1}{d_{hkl}^2} = \frac{1}{\sin^2 \beta}\left[\frac{h^2}{a^2} + \frac{k^2 \sin^2 \beta}{b^2} + \frac{l^2}{c^2} - \frac{2hl\cos\beta}{ac}\right]$$
Triclinic	$$\frac{1}{d_{hkl}^2} = \frac{1}{V^2}\left[h^2b^2c^2 \sin^2\alpha + k^2a^2c^2 \sin^2\beta + l^2a^2b^2 \sin^2\gamma \right.$$ $$+ 2hkabc^2(\cos\alpha\cos\beta - \cos\gamma) + 2kla^2bc(\cos\beta\cos\gamma - \cos\alpha)$$ $$\left. + 2hlab^2c(\cos\alpha\cos\gamma - \cos\beta)\right]$$ where $$V = abc\left[1 - \cos^2\alpha - \cos^2\beta - \cos^2\gamma + 2\cos\alpha\cos\beta\cos\gamma\right]^{\frac{1}{2}}$$

In a typical powder X-ray diffraction experiment, the sample is irradiated from a moving source and a moving detector measures the intensity of the diffracted X-rays, the measurements are carried out in the Bragg-Brentano geometry as a flat plate sample.

Powder diffraction data was collected using a Siemens D5000 instrument (Figure 2-6), utilising Cu-K$_\alpha$ radiation at room temperature. The samples were ground using a pestle and mortar in order to make sure that the crystals were randomly orientated. The powder was then mounted in a depression on the sample holder, and the surface flattened so that the level of the surface and the slide were consistent.

The patterns were collected using a step scan of size 0.02° 2θ over a 5–85° 2θ range and a step time of 0.8 seconds. When diffraction data was required for Rietveld refinement, higher intensities were needed. This was achieved by increasing the step time to 11 seconds and increasing the range from 5–105° 2θ. The patterns were compared to known patterns on the Inorganic Crystal Structure Database, (ICSD) or the Joint Committee on Powder Diffraction Standards, (JCPDS) database.
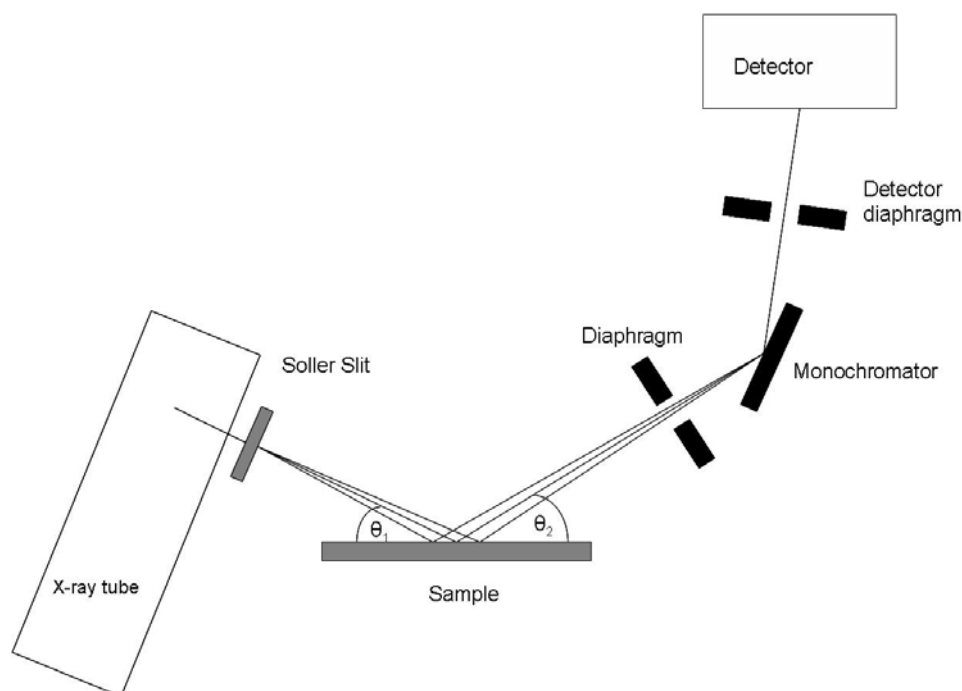
Figure 2-6: D5000 Schematic.
(The generator and detector move (θ$_1$ and θ$_2$) around a fixed sample giving 2θ readings).

Rietveld[53,54] refinements were carried out using the Generalised Structure Analysis Suite (GSAS)[55] and EXPGUI[56] software. The Rietveld method is a full profile refinement in which the powder pattern is fitted to a structural model. The process allows for accurate determination of cell dimensions, angles and atomic

positions. It includes preferred orientation and peak asymmetry in the refinement and also allows for multiple phases to be analysed and refined simultaneously.

The principle of the refinement process is to reduce a function M which represents the difference between a calculated profile $y^{(calc)}$ and the observed data $y^{(obs)}$. Rietveld described such an equation:

Equation 4: Where W_i is the statistical weight, c = overall scale factor such that $y^{calc} = cy^{obs}$.

$$M = \sum_i W_i \left\{ y_i^{obs} - \frac{1}{c} y_i^{calc} \right\}^2$$

The accuracy of the experimental to the calculated model is measured by a series of R factors, $R_{profile}$ (R_p), $R_{expected}$ (R_{exp}), $R_{weighted\ profile}$ (R_{wp}). The most meaningful of these mathematically is R_{wp} in which the numerator is the residual that is being minimised during the refinement.

Equation 5:
Where y_i = diffraction intensity.

$$R_{profile} = R_p = 100 \left[\frac{\sum_i |y_i(obs) - y_i(calc)|}{\sum y_i(obs)} \right]$$

Equation 6:
Where N = number of observations, P = number of refinable parameters, C = number of constraints and $w_i = 1/y_i$.

$$R_{expected} = R_{exp} = 100 \left[\sqrt{\frac{(N - C + P)}{\sum_i w_i [y_i(obs)]^2}} \right]$$

Equation 7

$$R_{weighted\ profile} = R_{wp} = 100 \sqrt{\left[\frac{\sum_i w_i [y_i(obs) - y_i(calc)]^2}{\sum_i w_i [y_i(obs)]^2} \right]}$$

2.3.2 Scanning Electron Microscopy

Scanning Electron Microscopy (SEM) in combination with Energy Dispersive X-rays (EDX) can be used to study the morphology, texture and surface features of a sample along with defining the elements associated with the interesting morphological features. The instrument set-up is shown in Figure 2-7. High resolution micrographs detailing the features can be produced for particles as small as 10nm although a working limit of 100nm is more realistic.
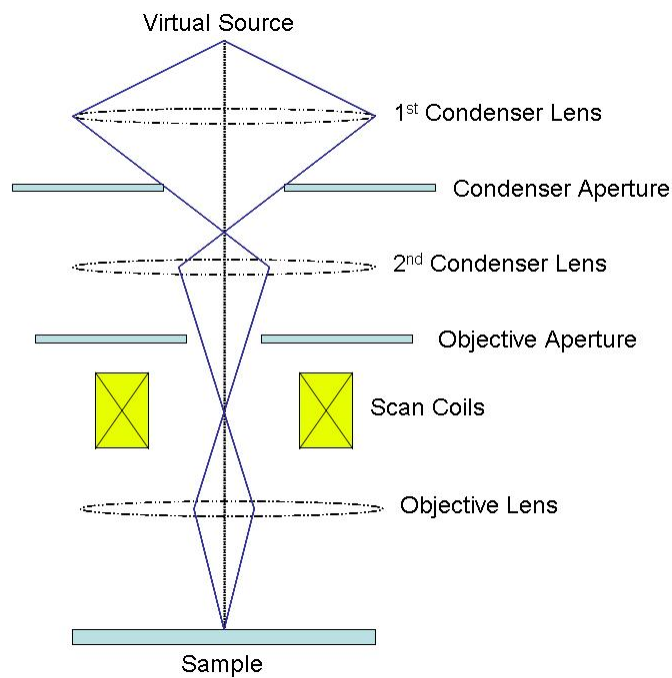
Figure 2-7: SEM Schematic.

The surface of the sample is analysed for both primary and secondary electrons as they are scattered or emitted from the surface. In the electron gun of a SEM, electrons are emitted from a tungsten filament and accelerated through a high voltage of 50-100kV. The electrons are focused to a small spot, between 50-100Å in diameter, on the sample surface using a condensing lens. The electron beam then scans the sample and two types of interaction can occur; an elastic collision and an inelastic collision, these are all shown in Figure 2-8.

Elastic collisions occur when the electrons in the beam hitting the samples bounce off at high energy (>50eV), which are detected at high angles. These are termed Back Scattered Electrons (BSE) and tend to scatter after penetrating deep into the sample. The degree of scattering is related to the number of electrons in the sample and hence the chemical composition.

Inelastic collisions occur when the electrons interact with the sample before emitting an electron. These, as a result, are low energy electrons (<50eV) and are detected at low angles. These are termed Secondary Electrons (SE) and as they come from the sample they have a higher surface detail than the BSE. Both interactions occur simultaneously within the microscope and the image can be obtained by selecting the detector. BSE imaging is useful particularly for non-conducting samples which cannot be imaged by SE due to the sample charging in the electron beam.
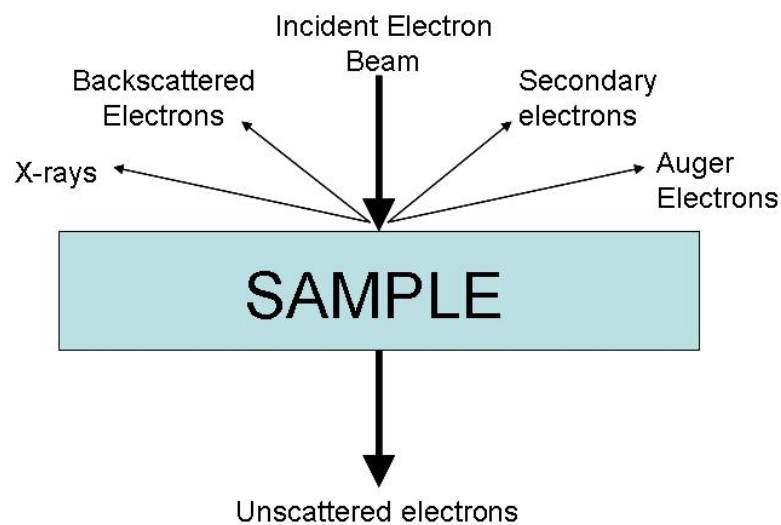
Figure 2-8: Scattering within a Scanning Electron Microscope.

The Auger effect which causes the emission of an electron from an atom initiates the emission of a second electron. When an electron is removed from a core level of an atom, leaving a vacancy, an electron from a higher energy level may fall into the vacancy, resulting in a release of energy. Although sometimes this energy is released in the form of an emitted photon, the energy can also be transferred to another electron, which is ejected from the atom. This second ejected electron is called an Auger electron.

EDX is a complementary technique, when a sample is bombarded with electrons which results in the emission of some X-rays. Electrons removed from low-lying orbitals create vacancies which can be filled by electrons of higher energy. The higher energy electrons that relax down into the vacancies will emit X-rays that are specific to the energy difference between the high and low energy state and therefore specific to the element that has emitted it. Elemental analysis on a small isolated part of a sample is theoretically possible. The results are displayed graphically and the peak heights seen are not directly related to the atomic ratio, as some atoms give much stronger signals than others but the instrument can interpret the data to give an approximate atomic ratio. The peak positions are assigned to the appropriate transition. Different atoms have different possible transitions depending on how the energy in the core electron shells (L, K and M) compare to the incident electrons. K lines are caused by X-rays emitted because of an electron dropping into a K level as shown by Figure 2-9, but L and M lines may also occur. However there are constraints to this hence a beryllium window is used to screen the detector from X-rays of higher energy, so that elements that have a lower atomic number than beryllium are not able to be assessed. Elements heavier than sodium can be routinely determined and in theory all elements from beryllium can be determined.

Samples were ground and a small amount of them scattered over a double-sided adhesive carbon mounted on an aluminium tab. Measurements were carried out using ultra-high vacuum.
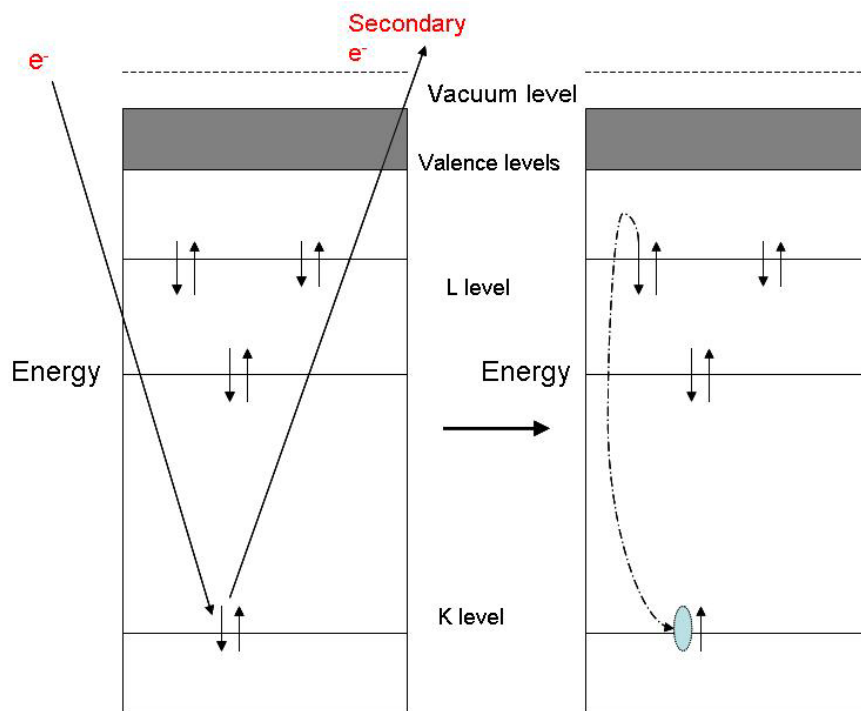
Figure 2-9: Energy level diagram involved in EDX.

2.3.3 Surface Area Determination

During the project surface area measurements were carried out on the samples. The surface area for catalysts is very important, as high surface areas can often lead to the possibility of increased catalytic activity which can enable the sample to be used for different applications.

The method of calculating the surface area was described by Brunauer, Emmett and Teller in 1938[57]. This was an expansion of the Langmuir theory for monolayer molecular adsorption, to multilayered adsorption using the hypotheses: (1) gas molecules adsorb infinitely on a solid in layers, (2) the first layer and second layer are seen as different to each other and subsequent layers are the same as the second layer, and (3) the Langmuir theory can be applied to each layer.

Equation 8: Where p and p_0 are the equilibrium and the saturation pressure of adsorbates at the temperature of adsorption, v_0 is the adsorbed gas volume, v_m is the volume of gas required to complete a unimolecular adsorbed layer, and c the BET constant

$$\frac{p}{v_0\left[p_0 - p\right]} = \frac{1}{v_m c} + \frac{c-1}{v_m c}\left(\frac{p}{p_0}\right)$$

Equation 9: Where R is the molar gas constant, T is the absolute temperature, E_1 is the heat of adsorption for the first layer and E_L is that for the second and higher layers and is equal to the heat of liquefaction

$$c = \exp\left(\frac{E_1 - E_L}{RT}\right)$$

The BET method is widely used in surface science for the calculation of surface areas of solids by physical adsorption of gas molecules. The total surface area S_{total} and specific surface area S are found through the equations:

Equation 10: Where N is Avogadro's number, s is the adsorption cross section, V is the molar volume of adsorbent gas and a is the weight of the sample.

$$S_{total} = \frac{\left(v_m N s\right)}{V}$$

$$S = \frac{S_{total}}{a}$$

There are various types of isotherms ranging from the type I isotherm as explained above and shown in Figure 2-10, to the type II and IV isotherms which are based on multiple layers as shown in Figure 2-11. Only types II and IV are used in the BET method. There are other isotherms such as types III, V and VI.
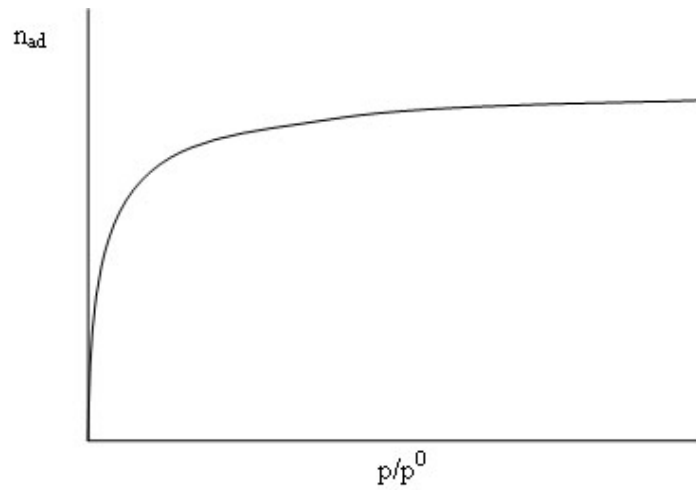
Figure 2-10: Type I isotherm.
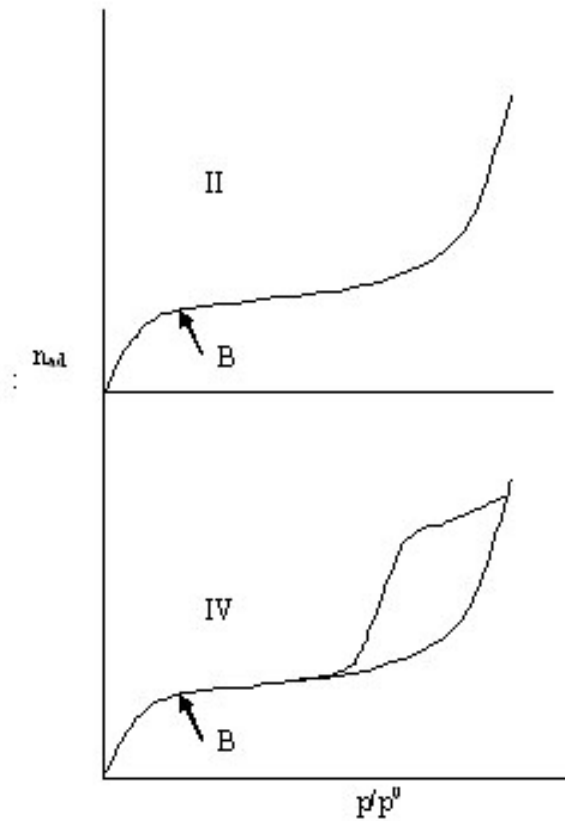
Figure 2-11: Type II and IV isotherms.

Type II isotherms are common for pore-free materials and are based on multilayer adsorption starting at point B. Type IV isotherms are similar to type II at low pressure however they show pore condensation at high pressure, they also show hysteresis as seen in Figure 2-11.

The surface areas of the samples during the project were determined by applying the (BET) method to nitrogen physisorption isotherms determined at liquid nitrogen temperatures. The isotherms were measured and displayed using a Micromeritics Flow Prep 060 and Gemini BET machine. The samples were degassed at $110^{o}C$ overnight to remove any adsorbed moisture prior to the analysis.

2.3.4 Elemental Analysis

CHN (Carbon, Hydrogen and Nitrogen) analysis was performed by Mrs Kim Wilson using a CE-440 elemental analyser. These results were used to analyse the amount of ammonia evolved during the reaction and to obtain a value for the amount of nitrogen present in the samples.

3 Lithium Molybdenum Oxide (Li₂MoO₄) – A Precursor to Lithium Molybdenum Nitride (LiMoN₂)

3 Lithium Molybdenum Oxide (Li_2MoO_4) – A Precursor to Lithium Molybdenum Nitride ($LiMoN_2$)

3.1 Introduction

Lithium molybdenum oxide (Li_2MoO_4) has been widely studied in the past with two structures being reported; either that of a rhombohedral cell of space group R-3[58], or a hexagonal $P3_2$[59] structure.

The formation of the R-3 form of the molybdate was reported to be through crystallisation of slowly cooled LiF-MoO_3 fluxes in platinum crucibles in air[58]. The structure was seen to crystallise into the structure type of the mineral phenacite (Be_2SiO_4), and therefore this polymorph of lithium molybdate is isostructural with lithium tungstate[60], as shown in Figure 3-1.
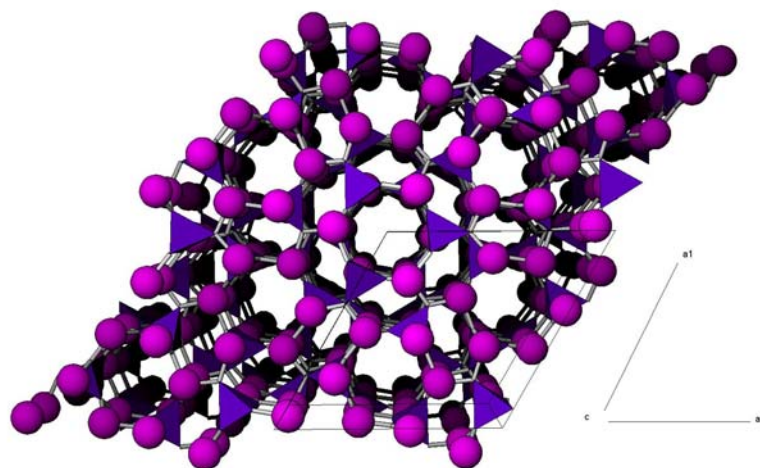
Figure 3-1: The R-3 polymorph of Lithium Molybdate, Li_2MoO_4.
Magenta spheres – Li, and purple tetrahedra – MoO_4.

The method synthesis of $P3_2$ lithium molybdate is not reported in the paper by Barinova et al.[59] although, it was stated that it was obtained from tiny well-faceted single crystals grown at the Institute of Physical Chemistry, Russian Academy of Sciences. The structure is as shown in Figure 3-2. Because of a lack of information about the synthetic route to the $P3_2$ structure it is hard to draw correlations between the synthetic process and the difference in structure of the two polymorphs. It can be seen that the polymorphs differ in the fact that they have a different centre of symmetry in the unit cell
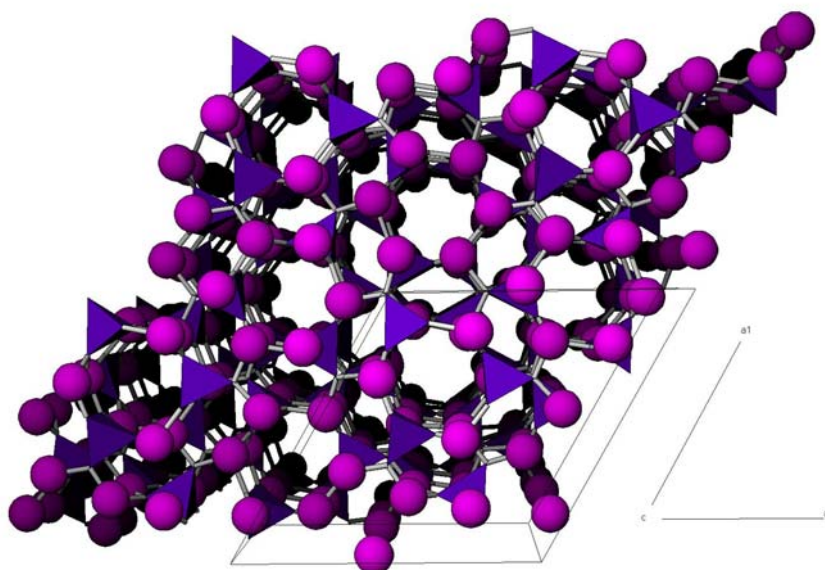
Figure 3-2: The $P3_2$ polymorph of Lithium Molybdate, Li_2MoO_4.
Magenta spheres – Li, and purple tetrahedra – MoO_4.

3.2 Experimental

Three synthetic routes were used to produce the molybdate, a high temperature synthesis following the method used by DiSalvo[18], a room temperature synthesis as described by Yip[51] and a precipitation reaction described by Inagaki[52].

Table 3-1: Masses of the relevant compounds.

Sample	Synthesised Temp (°C)	Mass (g)			
		MoO_3	Li_2CO_3	$LiOH·H_2O$	$(NH_4)_6Mo_7O_{24}·4H_2O$
1	650	2.484	1.275		
2	550	2.480	1.278		
3	550	2.481	1.271		
4	450	2.491	1.280		
5	500	2.487	1.274		
6	80			0.689	2.390
7	20	2.484		0.827	
8	500	2.497	1.272		
9	20	3.315		1.930	
10	20	3.272		1.918	
11	500	3.337	1.699		
12	20	3.324		1.939	
13	500	3.337	1.699		

N.B. Samples marked in blue were not formed in pure phase so they were not analysed further.

The high temperature synthetic route used a stoichiometric amount of lithium carbonate and molybdenum trioxide, as shown in Table 3-1. They were ground using a mortar and pestle and then heated in an alumina crucible for 18 hours to the temperature as shown and then cooled slowly. When conducted by DiSalvo[18] this synthesis was completed at 650°C. However during this project a range of temperatures from 500°C to 650°C was shown to produce the molybdate in pure phase after 18 hours of heating under air. Below 500°C the sample was shown to contain quantities of the starting materials molybdenum trioxide and lithium carbonate indicating that the minimum temperature limit for the production of the pure phase molybdate over the time scale chosen is around 500°C. The stoichiometric equation for the pathway occurring is given below:

$$MoO_{3(s)} + Li_2CO_{3(s)} \rightarrow Li_2MoO_{4(s)} + CO_{2(g)}$$
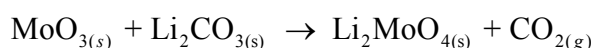
The room temperature synthesis described by Yip[51], uses a stoichiometric mixture of hydrated lithium hydroxide and molybdenum trioxide, as shown in Table 3-1, which is thoroughly ground using a mortar and pestle until a very fine paste forms. This paste is then dried at 100°C for 20 minutes, yielding the molybdate as shown below:

$$MoO_{3(s)} + 2LiOH \cdot H_2O_{(s)} \rightarrow Li_2MoO_{4(s)} + 3H_2O_{(l)}$$
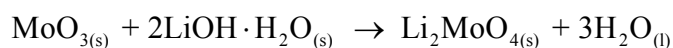
Further attempts to form the molybdate via the precipitation reaction first described by Inagaki[52], were unsuccessful. The process was multi-stage with ammonium molybdate salt and lithium hydroxide in solution, which was heated to around 80°C to remove the ammonia enriched solutes. The remaining solution was then dropped into ethanol which, with agitation, should have precipitated lithium molybdate. However attempts to synthesise the molybdate this way were not successful. Large amounts of water were required to dissolve the starting materials and a precipitate of the molybdate was not observed, even when the ethanol solution was cooled to induce precipitation. The expected process had been:

$$28LiOH \cdot H_2O_{(aq)} + 2(NH_4)_6 Mo_7O_{24} \cdot 4H_2O_{(aq)} \rightarrow 14Li_2MoO_{4(s)} + 12NH_{3(g)} + 56H_2O_{(l)}$$
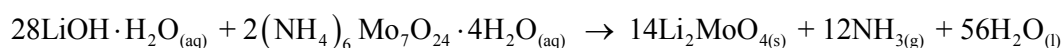
The samples obtained through the first two methods were characterised through powder X-ray diffraction, allowing for the comparison of the patterns with those of known samples previously recorded on the JCPDS or ICSD.

Powder diffraction data was collected using a Siemens D5000 instrument, utilising Cu-K$_\alpha$ radiation at room temperature. The samples were ground using a mortar and pestle in order to make sure that the crystals were randomly orientated. The powder was then mounted in a depression on sample holder, and the surface flattened so that the level of the surface and the slide was the same. As previously described in Section 2.3.1 the patterns were collected using a step scan of size 0.02° 2θ over a 5°–85° 2θ range and a time per step of 0.8 seconds. When diffraction data required for Rietveld refinements the step time and range was increased to 11 seconds and 5°–105° 2θ respectively.

A Phillips XL30 ESEM was used to examine the morphology and texture of the samples. As previously described in Section 2.3.2 the instrument was used in high vacuum with an operating voltage of 20kV, spot size of 4 and a working distance of 10mm. A secondary electron detector was used to obtain the images. To complement this, energy dispersive analysis by X-rays (EDX) was used to obtain the elemental composition of the sample.

The BET surface areas were measured using a Micromeritics Flow Prep 060 and Gemini BET machine. The samples were degassed at 110°C overnight to remove any adsorbed moisture prior to the analysis.

3.3 Results and Discussion

The samples were analysed using X-ray diffraction. The pattern shown in Figure 3-3 was matched to that for lithium molybdenum oxide (12-0763) on the JCPDS index. The method of synthesis in the matched pattern was by the crystallisation of a solution of lithium hydroxide and ammonium molybdate observed by the United States National Bureau of Standards[61]. The pattern was that of the R-3 polymorph with lattice parameters $a = b = 14.3368$Å, $c = 9.5889$Å; comparable with that of Kolitsch's work in which the parameters for the same polymorph was $a = b = 14.330(2)$Å, $c = 9.584(2)$Å[58].
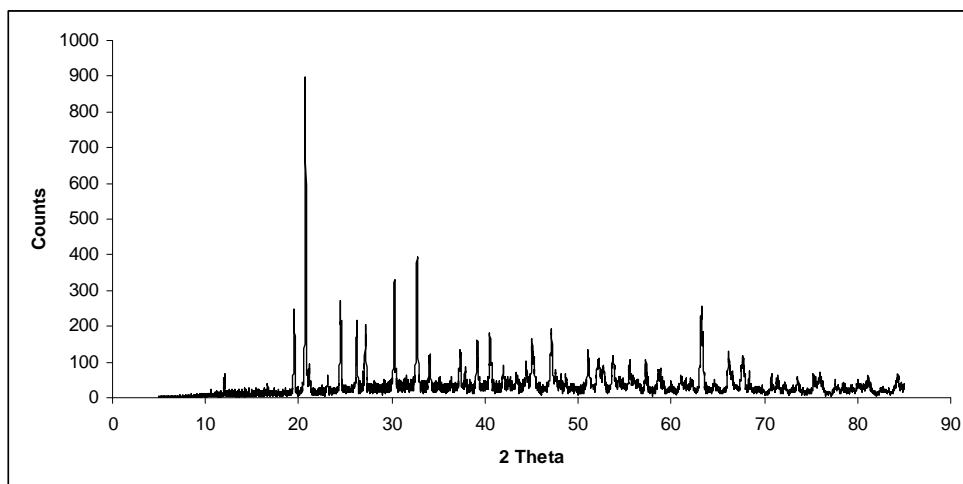
Figure 3-3: XRD pattern of Sample 10.
Lithium molybdate, Li_2MoO_4, prepared via the room temperature synthesis[51].

Figure 3-3 shows the XRD pattern of sample 10, collected over a short scan time, which is not conclusive enough to determine which polymorph of the molybdate is present. The $P3_2$ polymorph has characteristic reflections present at low 2θ values which are not present in the R-3 polymorph. However it was possible that high noise and background levels could be obscuring the low intensity reflections.

It would be possible to ascertain the correct polymorph by obtaining higher quality data from longer scans and then refining the patterns. The characteristic (200) and (11-1) reflections for the $P3_2$ polymorph are very weak in comparison to some of the other peaks (211) and (220) and so using a Rietveld quality scan reduces the background and sharpens any reflections present, so that phase identification is possible.

Using a scan time of 15 hours and a step time of 11 seconds per step it is possible to use the GSAS[55] programme to refine the structure and conclusively say what effect the synthetic methods had on the structure of lithium molybdate.

It was shown that after refinements, the XRD patterns could be accurately matched to that of the R-3 polymorph published by Kolitsch[58], with no sign of the characteristic reflections of the $P3_2$ polymorph. This suggests that the synthetic methods described in Section 3.1, will only form the R-3 polymorph.

The synthetic methods mentioned above for the R-3 polymorph have their limitations though, as the high temperature synthesis has only been shown to work between 500°C–650°C. Below 500°C the process is incomplete with impurities present in large quantities. Using the room temperature synthesis it is possible to produce the molybdate to the same purity without the need for prolonged heating. This leaves a large gap in the range over which the R-3 polymorph can be synthesised in its pure phase.

The observed difference plots (Figure 3-4, Figure 3-5 and Figure 3-6) and the related refined parameters (as described in Table 3-2, Table 3-3 and Table 3-4) show purity of the samples with only reflections matching those of lithium molybdate (Li_2MoO_4) present.

To make the refinements as reasonable as possible the oxygen atoms were constrained to refine the thermal parameter as the same value and the thermal parameters for the lithium atoms were fixed at a suitable value.

Figure 3-4: Final profile fit obtained from the X-ray diffraction data for Li_2MoO_4 (Sample 8). Sample prepared via the high temperature synthetic route at 500°C.
The observed data are crosses, the calculated profile the solid line and the lower continuous line the difference plot. Tick marks show allowed reflection positions.

Table 3-2: Sample 8 Refined parameters.
$\chi^2 = 1.782$ (50 Variables), R_{wp} (%) = 15.7, R_p (%) = 11.81;
R-3, $a = b$ = 14.33964(17) Å, c = 9.59257(13) Å.
‡ - Parameters fixed

Atoms	x	y	z	100x U_{iso}/U_{eq} (Å^2)
Li 1	0.1453(33)	0.4581(29)	0.2575(35)	1.00‡
Li 2	0.3082(32)	0.8435(30)	0.5880(37)	1.00‡
Mo	0.11797(14)	0.64681(13)	0.4151(4)	0.63*
O 1	-0.0044(9)	0.6614(13)	0.4363(20)	1.05(16)
O 2	0.2400(8)	0.7803(10)	0.4190(27)	1.05(16)
O 3	0.1211(10)	0.5785(11)	0.2547(25)	1.05(16)
O 4	0.1267(8)	0.5795(9)	0.5712(25)	1.05(16)

	U_{11} (Å^2)	U_{22} (Å^2)	U_{33} (Å^2)	U_{12} (Å^2)	U_{13} (Å^2)	U_{23} (Å^2)
Mo	0.37(13)	0.62(14)	0.67(11)	0.15(11)	-0.11(13)	0.21(16)
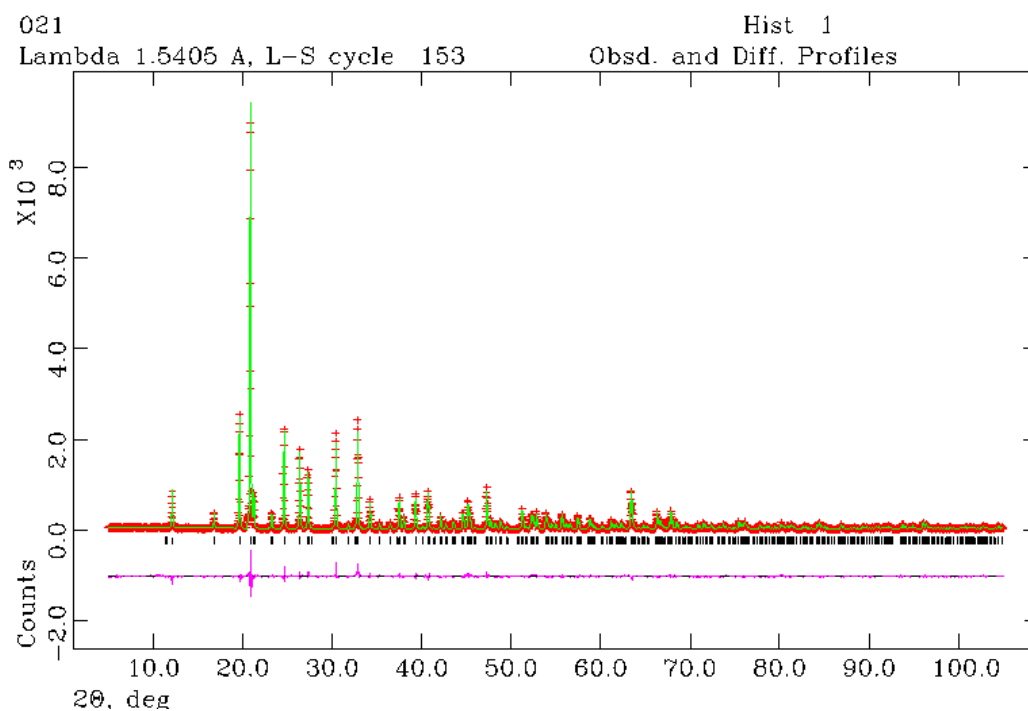
Figure 3-5: Final profile fit obtained from the X-ray diffraction data for Li$_2$MoO$_4$ (Sample 10). Sample prepared via the room temperature synthetic route.
The observed data are crosses, the calculated profile the solid line and the lower continuous line the difference plot. Tick marks show allowed reflection positions.

Table 3-3: Sample 10 Refined parameters.
χ^2 =1. 561 (49 Variables), R_{wp} (%) = 12.50, R_p (%) = 9.04;
R-3, $a = b$ = 14.33694(16) Å, c = 9.58906(13) Å.
‡ - Parameters fixed

Atoms	x	y	z	100x U_{iso} /U_{eq} (Å^2)
Li 1	0.1490(27)	0.4590(22)	0.229(10)	2.0‡
Li 2	0.3069(25)	0.8500(27)	0.556(10)	2.0‡
Mo	0.11828(11)	0.64700(11)	0.4168(5)	1.60*
O 1	0.0032(8)	0.6634(10)	0.4048(25)	2.16(14)
O 2	0.2367(7)	0.7777(8)	0.4242(24)	2.16(14)
O 3	0.1246(8)	0.5825(9)	0.2545(22)	2.16(14)
O 4	0.1252(7)	0.5817(8)	0.5686(23)	2.16(14)

	U_{11} (Å^2)	U_{22} (Å^2)	U_{33} (Å^2)	U_{12} (Å^2)	U_{13} (Å^2)	U_{23} (Å^2)
Mo	1.53(11)	1.63(11)	1.68(10)	0.89(9)	0.09(12)	0.06(14)
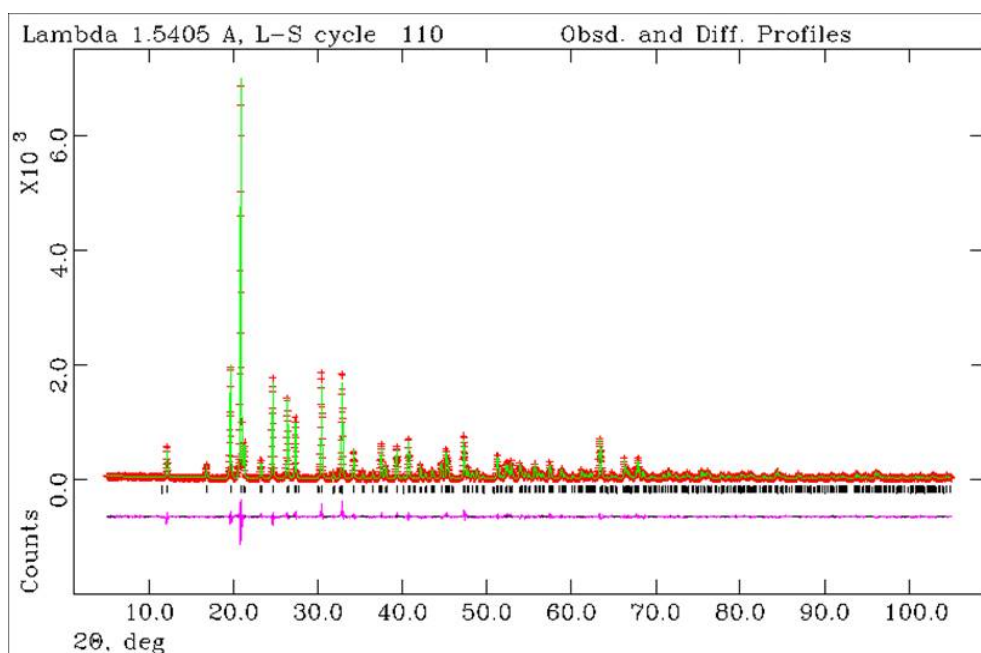
Figure 3-6: Final profile fit obtained from the X-ray diffraction data for Li_2MoO_4 (Sample 12).
Sample prepared via the room temperature synthetic route.
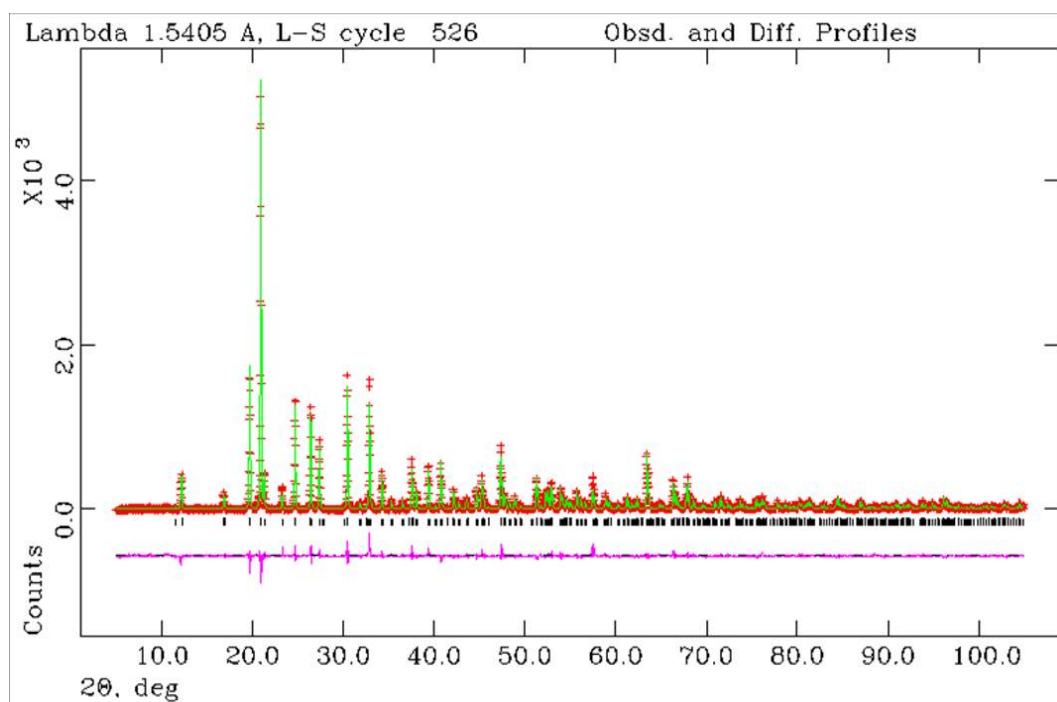The observed data are crosses, the calculated profile the solid line and the lower continuous line
the difference plot. Tick marks show allowed reflection positions.

Table 3-4: Sample 12 Refined parameters.
$\chi^2 = 1.735$ (49 Variables), R_{wp} (%) = 13.98, R_p (%) = 10.34;
R-3, $a = b = 14.33947(18)$ Å, $c = 9.59049(15)$ Å.
‡ - Parameters fixed

Atoms	x	y	z	100x U_{iso}/U_{eq} (Å^2)
Li 1	0.1473(30)	0.4614(26)	0.265(5)	1.50‡
Li 2	0.3069(29)	0.8472(26)	0.595(6)	1.50‡
Mo	0.11839(13)	0.64701(13)	0.4150(4)	1.34*
O 1	0.0021(9)	0.6628(11)	0.4051(25)	1.81(16)
O 2	0.2371(8)	0.7800(9)	0.4293(24)	1.81(16)
O 3	0.1266(10)	0.5830(10)	0.2480(22)	1.81(16)
O 4	0.1279(8)	0.5834(9)	0.5667(24)	1.81(16)

	U_{11} (Å^2)	U_{22} (Å^2)	U_{33} (Å^2)	U_{12} (Å^2)	U_{13} (Å^2)	U_{23} (Å^2)
Mo	1.02(12)	1.29(13)	1.52(11)	0.52(11)	0.14(13)	-0.01(16)

By comparing the bond length data collected as shown in Table 3-5 with those reported by Kolitsch (Table 3-6) it is possible to see how the synthesised samples are subtly different. Bond lengths differences show how the tetrahedra of LiO_4 are more compact in the samples prepared in the project than those reported by Kolitsch and vice versa for the MoO_4 tetrahedra.

Table 3-5: Selected Bond lengths of Li_2MoO_4 samples.

Sample 8		Sample 10		Sample 12	
Vector	Length (Å)	Vector	Length (Å)	Vector	Length (Å)
Li1-O1	2.02(4)	Li1-O1	2.107(28)	Li1-O1	2.034(33)
Li1-O2	1.87(4)	Li1-O2	2.04(4)	Li1-O2	1.86(4)
Li1-O3	1.92(4)	Li1-O3	1.937(27)	Li1-O3	1.916(29)
Li1-O3	1.96(4)	Li1-O3	1.77(4)	Li1-O3	1.97(4)
{Li1-O}	1.943	{Li1-O}	1.964	{Li1-O}	1.945
Li2-O1	2.03(4)	Li2-O1	1.961(30)	Li2-O1	2.005(32)
Li2-O2	1.88(4)	Li2-O2	1.81(4)	Li2-O2	1.93(4)
Li2-O4	1.90(4)	Li2-O4	1.994(25)	Li2-O4	2.023(32)
Li2-O4	1.88(4)	Li2-O4	1.96(4)	Li2-O4	1.78(4)
{Li2-O}	1.923	{Li2-O}	1.931	{Li2-O}	1.935
Mo1-O1	1.880(11)	Mo1-O1	1.801(10)	Mo1-O1	1.830(11)
Mo1-O2	1.838(10)	Mo1-O2	1.806(9)	Mo1-O2	1.812(10)
Mo1-O3	1.837(21)	Mo1-O3	1.857(14)	Mo1-O3	1.747(14)
Mo1-O4	1.819(21)	Mo1-O4	1.743(15)	Mo1-O4	1.895(16)
{Mo-O}	1.844	{Mo-O}	1.802	{Mo-O}	1.821

Table 3-6: Bond lengths adapted from ref. 58.

Vector	Length (Å)	Vector	Length (Å)
Li1-O2	1.947(4)	Li2-O2	1.942(4)
Li1-O3	1.954(3)	Li2-O1	1.949(4)
Li1-O1	1.956(3)	Li2-O4	1.975(4)
Li1-O3	2.003(4)	Li2-O4	2.002(4)
{Li1-O}	1.965	{Li2-O}	1.967
Mo-O1	1.7586(13)		
Mo-O2	1.7633(14)		
Mo-O3	1.7650(14)		
Mo-O4	1.7690(13)		
{Mo-O}	1.764		

The bond angles for the samples (Table 3-7) are in the same range as those reported by Kolitsch[58] suggesting that the tetrahedra of both LiO_4 and MoO_4 are also distorted in the samples made during the project. The LiO_4 tetrahedra show increased distortion with bond angles ranging from 98° to 125°.

This increased distortion and more compact framework, of both the LiO_4 and MoO_4 tetrahedra, gives a clearer view as to the difference in lattice parameters between those related to the refined patterns (as detailed previously) and the published values of $a = 14.330(2)$ Å, $c = 9.584(2)$ Å.

Table 3-7: Selected Bond angles for Li_2MoO_4 samples.

Sample 8		Sample 10		Sample 12	
Angle	**Degrees**	**Angle**	**Degrees**	**Angle**	**Degrees**
O1-Li1-O2	117.7(20)	O1-Li1-O2	104.1(17)	O1-Li1-O2	113.3(21)
O1-Li1-O3	101.9(20)	O1-Li1-O3	103.3(17)	O1-Li1-O3	106.8(18)
O1-Li1-O3	99.8(16)	O1-Li1-O3	105.0(20)	O1-Li1-O3	102.5(19)
O2-Li1-O3	111.0(19)	O2-Li1-O3	110.3(19)	O2-Li1-O3	108.1(17)
O2-Li1-O3	116.9(21)	O2-Li1-O3	121.2(17)	O2-Li1-O3	114.8(18)
O3-Li1-O3	108.0(18)	O3-Li1-O3	111.0(20)	O3-Li1-O3	111.0(19)
O1-Li2-O2	101.0(19)	O1-Li2-O2	113.4(21)	O1-Li2-O2	106.4(21)
O1-Li2-O4	98.9(19)	O1-Li2-O4	103.3(16)	O1-Li2-O4	98.9(17)
O1-Li2-O4	111.3(18)	O1-Li2-O4	105.3(20)	O1-Li2-O4	111.3(22)
O2-Li2-O4	106.4(18)	O2-Li2-O4	107.9(19)	O2-Li2-O4	108.9(18)
O2-Li2-O4	122.6(22)	O2-Li2-O4	117.2(17)	O2-Li2-O4	124.8(20)
O4-Li2-O4	113.5(20)	O4-Li2-O4	108.8(18)	O4-Li2-O4	103.5(19)
O1-Mo1-O2	109.7(6)	O1-Mo1-O2	108.6(6)	O1-Mo1-O2	109.8(6)
O1-Mo1-O3	115.0(7)	O1-Mo1-O3	109.3(11)	O1-Mo1-O3	114.9(12)
O1-Mo1-O4	106.6(7)	O1-Mo1-O4	111.5(11)	O1-Mo1-O4	106.8(12)
O2-Mo1-O3	107.9(7)	O2-Mo1-O3	108.8(6)	O2-Mo1-O3	103.1(6)
O2-Mo1-O4	104.7(7)	O2-Mo1-O4	101.5(6)	O2-Mo1-O4	106.5(6)
O3-Mo1-O4	112.3(5)	O3-Mo1-O4	116.7(4)	O3-Mo1-O4	115.4(4)

From the SEM micrographs it is possible to see the size and morphology of the samples. The images show that the molybdate samples have a very varied structure within the small amount viewed on the SEM, with the particles ranging from clusters of small particulates to larger angular particles as seen in Figure 3-7 and Figure 3-8.
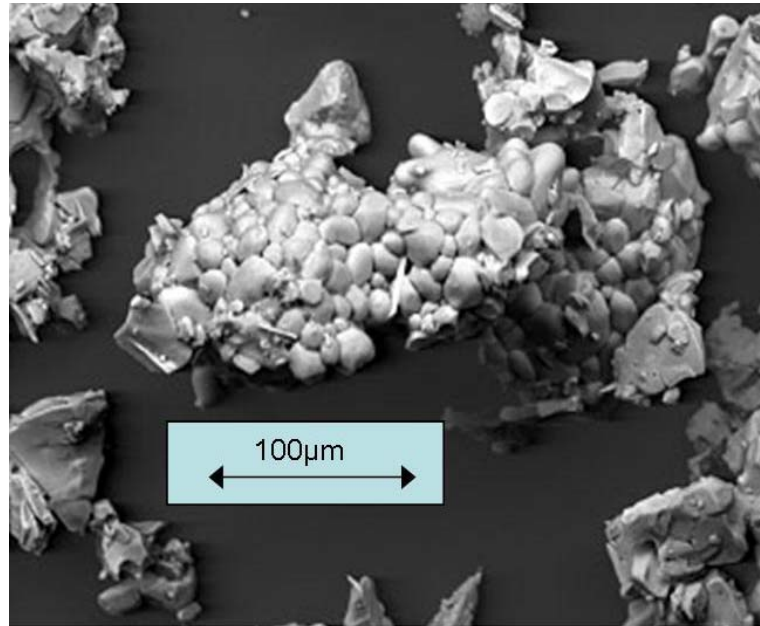
Figure 3-7: SEM image of Li_2MoO_4 (Sample 2).
Sample prepared via the high temperature synthetic route.
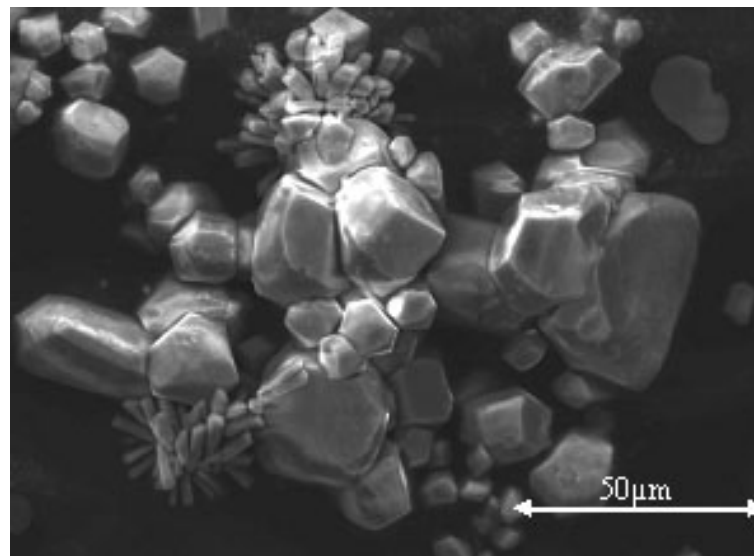
Figure 3-8: SEM image of Li_2MoO_4 (Sample 2).
Sample prepared via the high temperature synthetic route.

The samples made through the high temperature method are all very comparable and the particles in the selected area scan show similar morphology with a combination of the rounded and angular particles throughout the samples and a variation in size of particulates from 30 μm to 50μm approximately.

Using Energy Dispersive X-ray analysis (EDX) taken over numerous different spot scans, it is possible to show that the particles contain molybdenum and oxygen. Lithium cannot be detected using EDX.

Table 3-8: EDX data for different points on Sample 2 taken from Figure 3-7.

Ratio	Mo	1.03	1.14	1.06	0.98
	O	3.87	4.21	4.13	4.05

The ratio between Mo and O for the K-peaks was seen as shown in Table 3-8 to be a 1:4 Mo:O suggesting that the molybdate (Li_2MoO_4) as observed by XRD is present. This evidence, along with that of the XRD patterns, suggests the molybdate is pure phase throughout each of the samples.

For the molybdates synthesised at room temperature, the SEM images show very small scale particles with no evidence of the large scale particles seen for the lithium molybdates formed at higher temperatures, as shown previously. The particles as seen in Figure 3-9 and Figure 3-10 are of a few microns in length in contrast to the 50 micron particles seen when the molybdate is formed at temperatures between 500°C and 650°C.
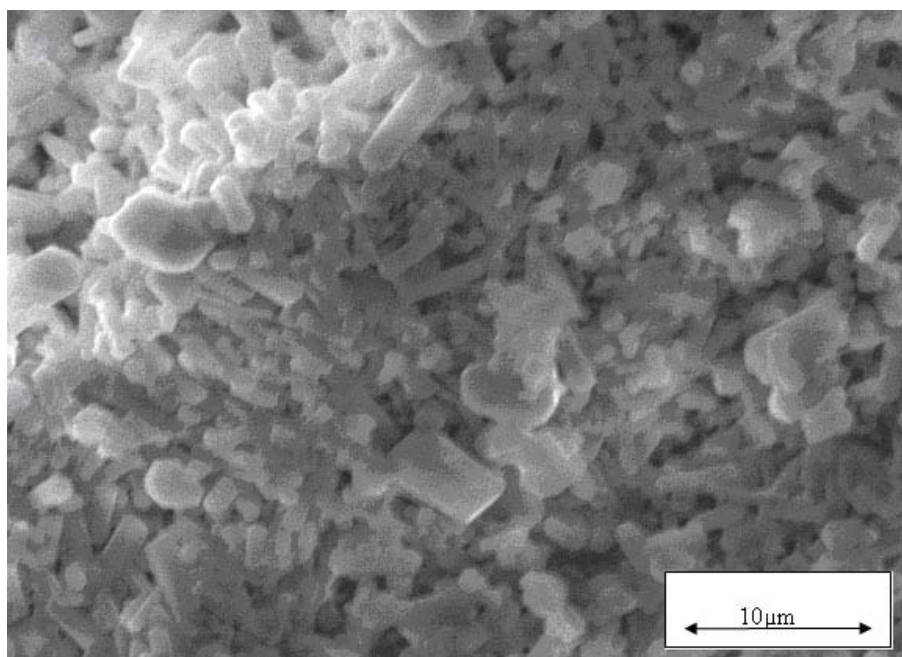
Figure 3-9: SEM image of Li_2MoO_4 (Sample 12).
Sample prepared via the room temperature synthetic route.
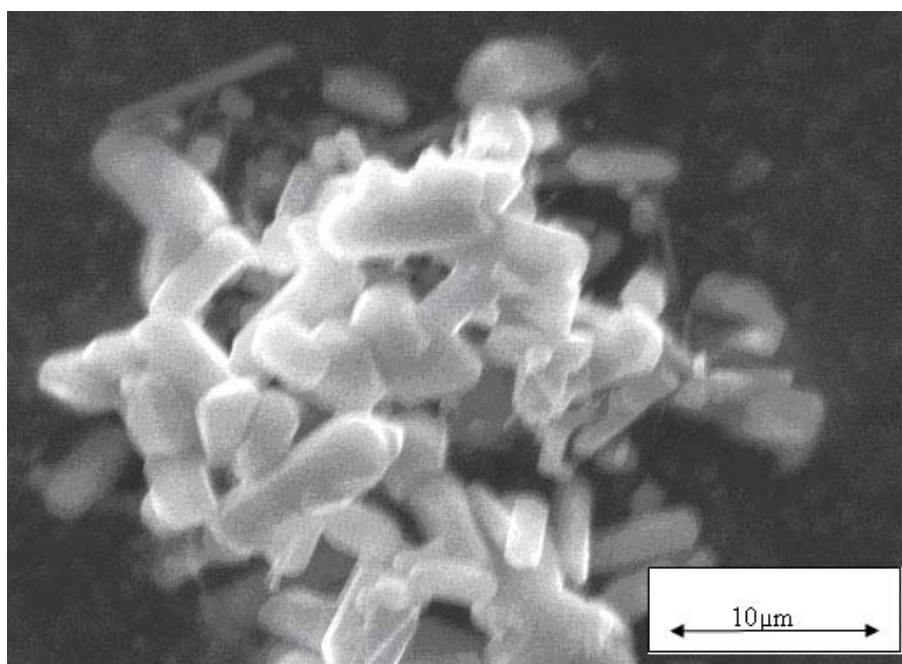
Figure 3-10: SEM image of Li_2MoO_4 (Sample 12).
Sample prepared via the room temperature synthetic route.

Due to technical problems with the instrument at the time of measurement it was not possible to collect EDX data for these samples. Hence the ability to confirm the composition of the crystals in the above figures was limited.

The surface areas of the molybdates formed via the two synthetic methods were very similar with the samples prepared at room temperature, having a surface area

of ca. $5m^2g^{-1}$, compared with that of the high temperature synthesis which had a surface area of ca. $3.5m^2g^{-1}$.

With two polymorphs (R-3 and $P3_2$) of lithium molybdate possible to be synthesised via various methods as described in previous work[58,59], studies were carried out to see if conversion between the two polymorphs was possible and most interestingly if the R-3 polymorph could be converted to the $P3_2$ polymorph. If this was possible it would show conversion from a simpler symmetry to a more complex symmetry.

Initially thermal analysis was conducted using a Netzch STA 409 PC, which is a highly sensitive balance which allows for small weight loss to be observed with heating. The profile uses a heating rate of 10°C/min up to 800°C. Over this time a small mass loss of 1.7% was observed, which could be assigned to the loss of waters of crystallisation from the sample. The other major event that occurred could be assigned to the melting point for Li_2MoO_4 however this started around 15°C before the reported melting point of 705°C so could be associated with the melting process (just prior to complete melting). The temperature profile is shown in the trace (Figure 3-11).
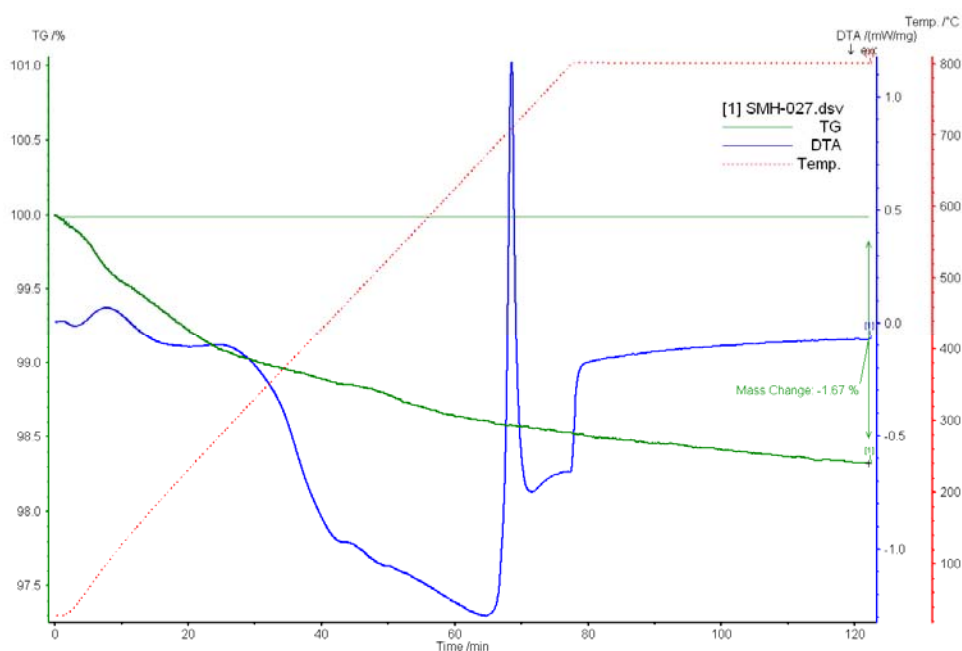
Figure 3-11: STA trace of Li_2MoO_4.
Sample prepared via the room temperature synthetic route.
The trace shows the loss of waters of crystallisation and the melting point of the lithium molybdate at 705°C.

To further explore the effect of the temperature, the molybdate was analysed using variable temperature XRD, which allowed for the sample to be heated and analysed *in-situ*. The temperature was raised to 700°C over an extended period of time to allow for high quality X-ray diffraction patterns to be obtained. The resultant patterns which were obtained in the region 10 - 32° 2θ (within which the characteristic (200) and (11-1) reflections of the P3$_2$ polymorph are found) are shown in Figure 3-12.
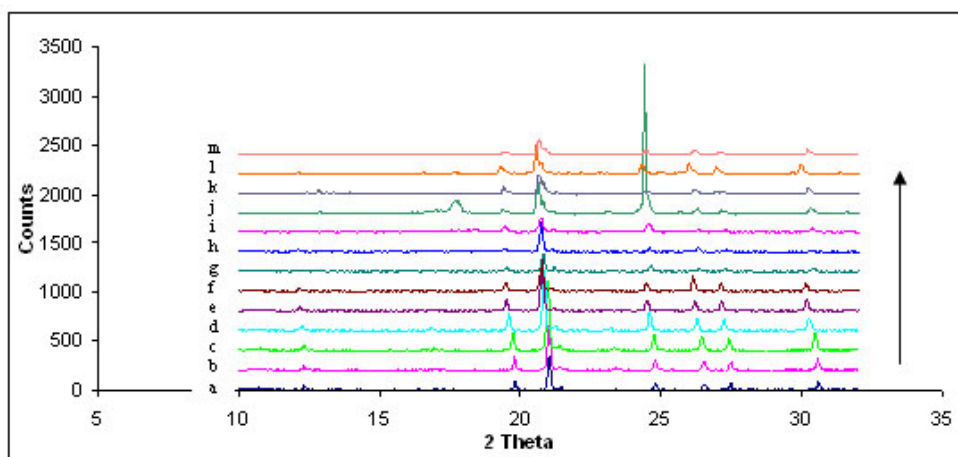
Figure 3-12: Variable temperature XRD patterns of the R-3 polymorph of lithium molybdate. a = 30°C, b = 100°C, c = 300°C, d = 500°C, e = 600°C, f = 620°C, g = 640°C, h = 645°C, i = 655°C, j = 660°C, k = 700°C, l = 500°C, m = 30°C after cooling.

As the temperature was increased in the XRD there was a thermal expansion of the unit cell which can be easily seen in the shift of the Bragg reflections to a lower 2θ value (Figure 3-13).
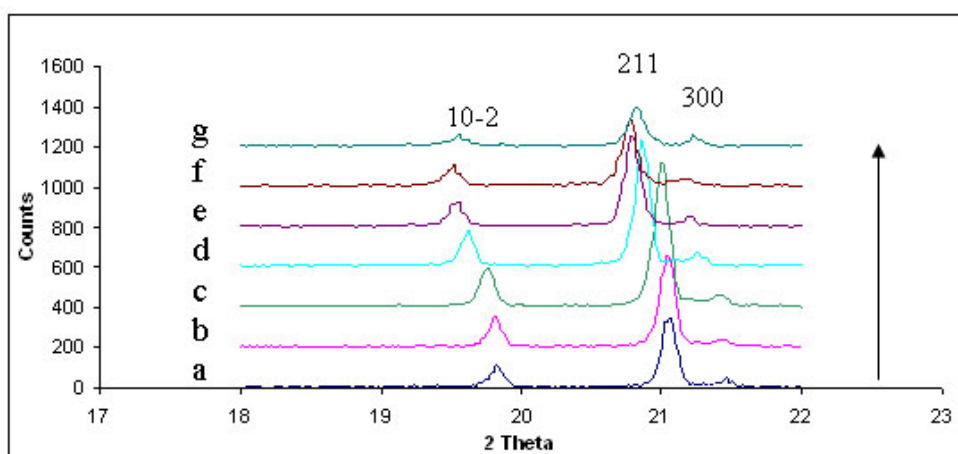
Figure 3-13: Patterns showing shift of (10-2) peak with increasing temperature. a = 30°C, b = 100°C, c = 300°C, d = 500°C, e = 600°C, f = 620°C, g = 640°C.

After 660°C there is a formation of a reflection at 17° 2θ and an enlargement of the (220) reflection (as seen in Figure 3-12), due to the formation of Li$_2$MoO$_3$.

After 700°C the pattern has a reduced intensity but is still able to be matched to the R-3 polymorph of Li_2MoO_4. This can be seen in the two patterns taken at 500°C and 30°C on cooling in Figure 3-12. The melting point of lithium molybdate (Li_2MoO_4) is 705°C and this could be assigned to the changes at around 700°C which afterwards shows a very weak series of reflections related to the molybdate.

The variable temperature XRD showed that the R-3 polymorph was not converted to the $P3_2$ polymorph on heating. This suggests that converting between the two polymorphs is not possible and that the events seen in the STA trace at 700°C are due to the melting of the sample. This is confirmed by the XRD patterns which show a broadening and weakening of the reflections.

3.4 Summary

From the data collected, it is possible to say that the lithium molybdate (Li_2MoO_4) can be formed as a pure phase via two different methods. The high temperature synthesis reacting lithium carbonate and molybdenum trioxide produces the R-3 polymorph of lithium molybdate. This polymorph however can also be formed by the room temperature preparation using mono-hydrated lithium hydroxide and molybdenum trioxide which, when ground together, form a paste with the help of the waters of crystallisation.

The possibility of conversion between the two polymorphs (R-3 and $P3_2$) has not been shown under the conditions used during this work, with only the R-3 polymorph[58] observed via XRD. This however does not conclusively mean that conversion between the two is not possible as the synthetic route to the $P3_2$ polymorph[59] has not been reported.

Both methods (as previously described) give the pure phase R-3 lithium molybdate, however the room temperature preparation gives a much more crystalline product than the higher temperature preparation.

However the SEM images show a distinct difference. The high temperature molybdates are seen to be made up of larger scale particles with very angular edges as opposed to those seen in the room temperature preparation which are

smaller and resemble a tube or rod like structure. The surface areas of the molybdates are both very small with an average surface area for the high temperature samples of 3.5 m^2g^{-1} compared to the slightly higher 5 m^2g^{-1} for the room temperature synthesised samples.

Hence all of the evidence seen in the X-ray diffraction and the SEM images and EDX show that the molybdate formed is always that of the R-3 polymorph as proposed by Kolitsch[58]. The polymorph has been shown by variable temperature diffraction to expand up to a temperature of approximately 600°C and then at approximately 660°C Li_2MoO_3 is formed. This is only seen briefly and is then followed by the melting of the molybdate at 705°C. The EDX of the samples all confirm the presence of four oxygen atoms for every molybdenum atom.

With all of the data collected it can be shown that lithium molybdate (Li_2MoO_4) can be formed via two different methods to give very pure samples with no impurity phases. Both methods of synthesis give the R-3 polymorph under the conditions used in the project.

4 Lithium Molybdenum Nitride (LiMoN₂)

4.1 Introduction

As previously described in section 1.1.4, the synthesis of lithium molybdenum nitride was first reported in 1992 by DiSalvo *et al.*[18]. When analysed, the resultant nitride was found to contain an impurity of lithia (Li_2O). The presence of both lithium molybdenum nitride and lithia showed that the reaction proceeds as expected with the reaction following the pathway:

$$Li_2MoO_{4(s)} + \frac{7}{3}NH_{3(g)} \rightarrow LiMoN_{2(s)} + \frac{1}{2}Li_2O_{(s)} + \frac{1}{6}N_{2(g)} + \frac{7}{2}H_2O_{(g)}$$
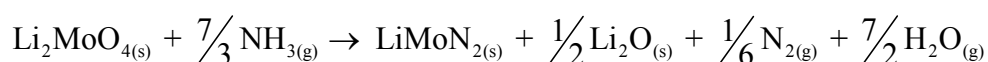
DiSalvo *et al.* also proposed that another impurity present was γ-Mo₂N which was excluded from the refinement of the neutron diffraction data they published. The molybdenum nitride is possibly formed from a reaction of incompletely reacted molybdenum trioxide left from the starting molybdate. This would form γ-Mo₂N on exposure to NH_3, as seen in previous work conducted on MoO_3[62]. Alternatively it could be formed from the decomposition of LiMoN₂.

Another method of preparation could be via the ammoniation of lithium molybdenum sulfide which although not shown directly for LiMoN₂, has been shown to work for the analogous lithium tungsten nitride LiWN₂ system[19].

4.2 Experimental

The nitride was formed by the ammonolysis of lithium molybdenum oxide (Li_2MoO_4) inside a tube furnace with the molybdate in an alumina boat over which a flow of ammonia (10mlmin⁻¹) was passed for 14 hours at 710°C. This process follows the method described by DiSalvo[18]. The ammonolysis was also conducted in a silica tube for 14 hours at 710°C but at 90mlmin⁻¹, this follows the method employed by Aika[41] and McKay[46] which uses a plug-flow regime. The regime used is shown in Table 4-1.

Table 4-1: Precursor samples nitrided at 710°C to give lithium molybdenum nitride.

Sample	Precursor Synthesised Temp (°C)	Nitrided under		
		NH$_3$	NH$_3$ (Plug-flow)	25% N$_2$/H$_2$
1	650	√		
2	550	√		
3	550	√		
5	500	√		
8	500	√		
10	20	√		
11	500		√	
12	20	√		
13	500			√

The samples were characterised through powder X-ray diffraction and compared to the patterns of known samples previously recorded in the JCPDS or ICSD.

Powder diffraction data was collected using a Siemens D5000 instrument, utilising Cu-K$_\alpha$ radiation at room temperature. The samples were ground using a mortar and pestle in order to make sure that the crystals were randomly orientated. The powder was then mounted in a depression on sample holder, and the surface flattened so that the level of the surface and the slide was the same. As previously described in Section 2.3.1 the patterns were collected using a step scan of size 0.02° 2θ over a 5°–85° 2θ range and a time per step of 0.8 seconds. When diffraction data required for Rietveld refinements the step time and range was increased to 11 seconds and 5°–105° 2θ respectively.

A Phillips XL30 ESEM was used to examine the morphology and texture of the samples. As previously described in Section 2.3.2 the instrument was used in high vacuum with an operating voltage of 20kV, spot size of 4 and a working distance of 10mm. A secondary electron detector was used to obtain the images. To complement this, energy dispersive analysis by X-rays (EDX) was used to obtain the elemental composition of the sample.

The BET surface areas were measured using a Micromeritics Flow Prep 060 and Gemini BET machine. The samples were degassed at 110°C overnight to remove any adsorbed moisture prior to the analysis.

4.3   Results and Discussion

The samples were analysed using X-ray diffraction, initially over a one hour scan to identify the phases present. The patterns recorded after a one hour scan were very noisy with a large background reading and extra reflections, indicating some form of impurity present in the sample.
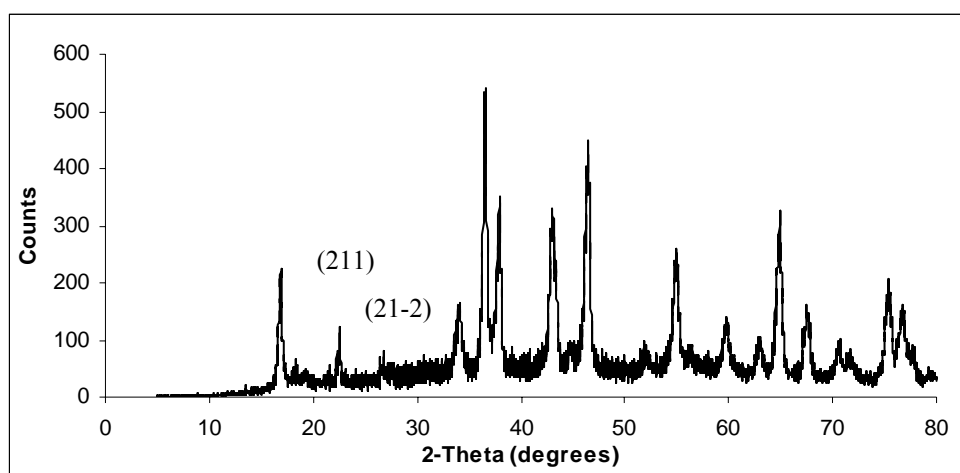
Figure 4-1: XRD pattern of Sample 8.
Sample prepared via the high temperature synthetic route.
Showing the presence of impurities (lithium molybdate remaining from the precursor stage).

Figure 4-1 shows how the amorphous background and the extra reflections between 20 and 30° 2θ, do not allow for the sample to be fully characterised as the amorphous background could be obscuring reflections relating to other impurities. The scan does allow for the main phase, $LiMoN_2$, to be identified along with the strong reflections (211) and (21-2) of Li_2MoO_4.

The exact nature of the impurities varied from sample to sample, lithia was always present as per the reaction scheme proposed by DiSalvo[18]; however the molybdate content was variable.

Elemental analysis of the samples showed a sub-stoichiometric amount of nitrogen present. This cannot be conclusively attributed to a lack of nitrogen in the $LiMoN_2$ due to the impurities present in each sample (lithia and lithium molybdate). However, based on calculations from the elemental analysis the nitrides, were still showing a sub-stoichiometric amount of nitrogen present, with the samples produced at higher temperatures as shown in Table 4-2.

Table 4-2: Elemental analysis showing percentage of N in the samples.

Sample	Wt % Nitrogen	% of Expected Nitrogen content*	Assumed stoichiometry
1	12.30	74%	"LiMoN$_{1.48}$"
3	13.04	78%	"LiMoN$_{1.56}$"
5	12.54	75%	"LiMoN$_{1.5}$"
8	11.52	69%	"LiMoN$_{1.38}$"
10	10.58	63%	"LiMoN$_{1.26}$"
12	9.00	54%	"LiMoN$_{1.08}$"

*Calculated from the weight % of nitrogen present in the sample and the expected amount of nitrogen.
N.B.: Loadings and stoichiometry based on the presence of LiMoN$_2$ and Li$_2$O.

However the XRD patterns showed no variation from the recorded pattern of LiMoN$_2$ recorded by DiSalvo. This suggests that there may be other impurities present in the samples which were not being accounted for in the calculations used to obtain the loading and assumed stoichiometry. This would have the effect of reducing the stoichiometry of the nitrides without altering the pattern obtained from XRD.

In an attempt to try and identify other impurities in the sample, a longer scan time was used (previously used to indentify the lithium molybdate) in order to refine and fully characterise the samples. The refined patterns are shown in Figure 4-2 and Figure 4-3 and the respective data in Table 4-3 and Table 4-4.

To make the refinements as reasonable as possible the lithium and molybdenum atoms as they are site sharing are constrained to be refined to the same values for position and thermal parameters and the nitrogen atoms were constrained to refine the thermal parameter to the same value. The same constraints were used for the molybdate as described previously.
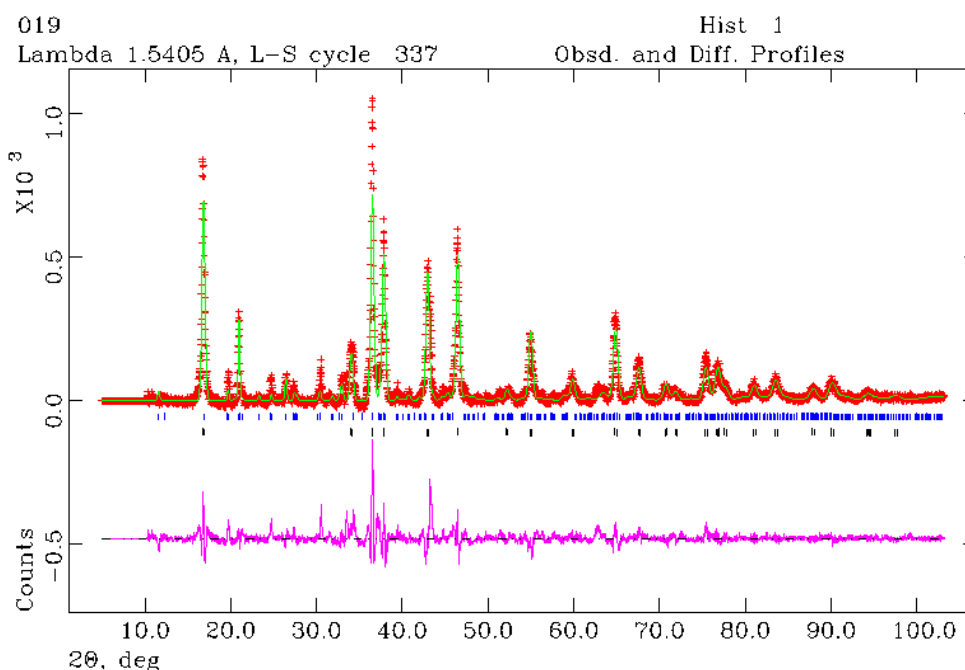
Figure 4-2: Final profile fit obtained from the X-ray diffraction data for $LiMoN_2$ (Sample 8). The observed data are crosses, the calculated profile the solid line and the lower continuous line the difference plot. Tick marks show allowed reflection positions.

Table 4-3: Sample 8 Refined parameters.
$\chi^2 = 3.083$ (45 variables), $R_{wp}(\%) = 20.28$, $R_p(\%) = 15.87$;
‡ - Parameters fixed
Lithium Molybdenum Nitride; R3m, $a = b = 2.87088(22)$ Å, $c = 15.7405(20)$ Å.

Atoms	x	y	z	Occupancy	100x U_{iso}/U_{eq} (Å^2)
Li 1	0.0	0.0	-0.0029(9)	0.85‡	0.74(9)
Mo 1	0.0	0.0	-0.0029(9)	0.15‡	0.74(9)
Li 2	0.0	0.0	0.819738	0.15‡	0.71(31)
Mo 2	0.0	0.0	0.819738	0.85‡	0.71(31)
N 1	0.0	0.0	0.2546(20)	1‡	0.54‡
N 2	0.0	0.0	0.4209(15)	1‡	0.54‡

Lithia: Fm-3m, $a = b = c = 4.6230(1)$ Å

	x	y	z	Occupancy	100x U_{iso}/U_{eq} (Å^2)
Li 1	0.0	0.0	0.0	1‡	0.25‡
O 1	0.25	0.25	0.25	1‡	0.25‡

Lithium Molybdenum Oxide (Li_2MoO_4); R-3, $a = b = 14.358(4)$ Å, $c = 9.643(4)$ Å

|	x	y	z	Occupancy	100x U_{iso}/U_{eq} (Å^2)
Li 1	0.1411(2)	0.4550(2)	0.2532(2)	1‡	0.90‡
Li 2	0.3090(2)	0.8562(2)	0.5823(2)	1‡	0.90‡
Mo 1	0.1379(17)	0.6622(24)	0.3867(16)	1‡	0.75(3)
O 1	-0.0401(2)	0.5569(2)	0.3968(6)	1‡	0.80‡
O 2	0.3379(2)	0.6750(10)	0.5957(8)	1‡	0.80‡
O 3	-0.0664(9)	0.3454(10)	-0.2271(4)	1‡	0.80‡
O 4	0.1337(7)	0.5752(4)	0.5740(2)	1‡	0.80‡
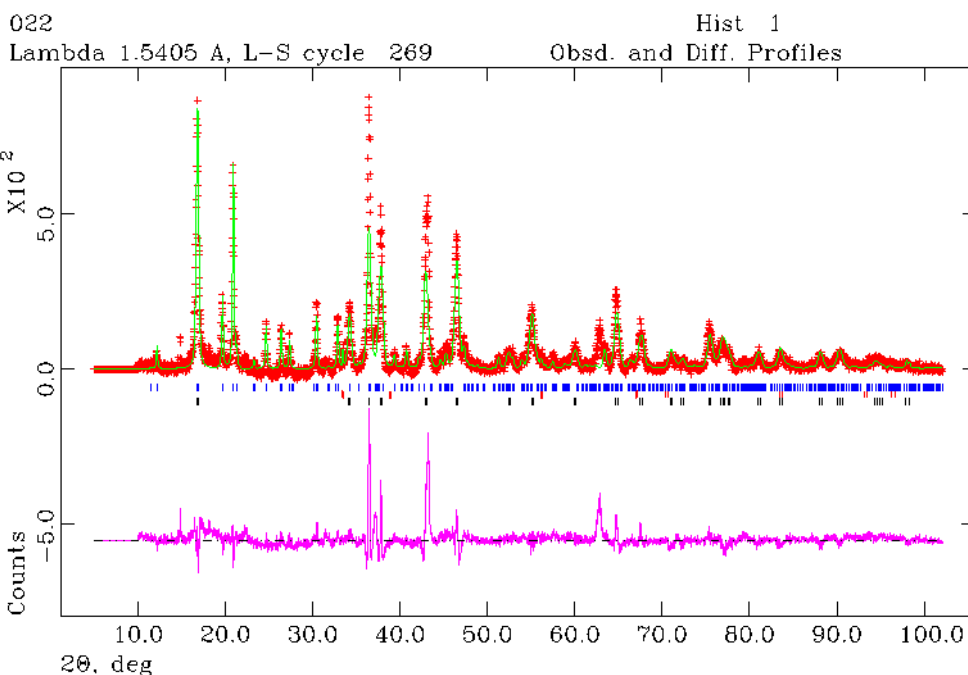
Figure 4-3: Final profile fit obtained from the X-ray diffraction data for LiMoN$_2$ (Sample 10). The observed data are crosses, the calculated profile the solid line and the lower continuous line the difference plot. Tick marks show allowed reflection positions.

Table 4-4: Sample 10 Refined parameters.
χ^2 = 4.241 (26 Variables), R$_{wp}$ (%) = 22.01, R$_p$ (%) = 16.81;
‡ - Parameters fixed
Lithium Molybdenum Nitride; R3m, $a = b$ = 2.87131(27) Å, c = 15.6528(24) Å.

Atoms	x	y	z	Occupancy
Li 1	0.0	0.0	0.02613(6)	0.85‡
Mo 1	0.0	0.0	0.02613(6)	0.15‡
Li 2	0.0	0.0	0.8453(11)	0.15‡
Mo 2	0.0	0.0	0.8453(11)	0.85‡
N 1	0.0	0.0	0.2864(17)	1‡
N 2	0.0	0.0	0.4495(16)	1‡

Lithia: Fm-3m, $a = b = c$ = 4.6213(16) Å

Li 1	0.0	0.0	0.0	1‡
O 1	0.25	0.25	0.25	1‡

Lithium Molybdenum Oxide (Li$_2$MoO$_4$); R-3, $a = b$ = 14.3539(29) Å, c = 9.6003(23) Å

Li 1	0.141(28)	0.455(28)	0.25(7)	1‡
Li 2	0.309(20)	0.856(30)	0.58(7)	1‡
Mo 1	0.1198(11)	0.6490(12)	0.420(4)	1‡
O 1	0.0052(3)	0.6646(7)	0.41520(1)	1‡
O 2	0.2336(6)	0.7768(6)	0.41607 (7)	1‡
O 3	0.1192(5)	0.5789(1)	0.26342(2)	1‡
O 4	0.1190(7)	0.5781(3)	0.56859(9)	1‡

The refinements show that the nitride has residual molybdate reflections remaining in the sample and that the lithia proposed in the reaction profile is also present. The phase fractions shown in Table 4-5 give an idea of the quantity of impurities present in the samples.

Table 4-5: Phase fractions from refined samples. (Weight Fractions)

Phase	Sample	
	8	10
$LiMoN_2$	0.10765×10^{-5}	0.67809
Li_2O	1	0.05334
Li_2MoO_4	0.13120×10^{-6}	0.26857

Comparing the bond lengths and angles of the synthesised samples (Table 4-6 and Table 4-7) with those published by DiSalvo (Table 4-8) show how very different the structures are − with the published bond lengths being consistent between the Mo-N and the Li-N. However this is not the case with the samples synthesised from both room temperature and higher temperatures, where the bond lengths are varied and shows a distortion in the structure. This is also seen in the bond angles which are very different for the samples synthesised and the literature results.

Table 4-6: Selected bond lengths $LiMoN_2$.

8		10	
Vector	Length (Å)	Vector	Length (Å)
Mo1-N1 (x3)	2.043(13)	Mo1-N1 (x3)	2.014(15)
Mo1-N2 (x3)	2.178(15)	Mo1-N2 (x3)	2.176(16)
Li1-N1 (x3)	2.043(13)	Li1-N1 (x3)	2.014(15)
Li1-N2 (x3)	2.178(15)	Li1-N2 (x3)	2.176(16)

Table 4-7: Selected bond angles for LiMoN$_2$.

Angle	Degrees	Angle	Degrees
N1-Mo1-N1 (x3)	89.3(7)	N1-Mo1-N1 (x3)	90.9(9)
N1-Mo1-N2 (x3)	76.2(7)	N1-Mo1-N2 (x3)	75.0(8)
N1-Mo1-N2 (x6)	133.46(24)	N1-Mo1-N2 (x6)	132.95(29)
N1-Li1-N1 (x3)	89.3(7)	N1-Li1-N1 (x3)	90.9(9)
N1-Li1-N2 (x3)	76.2(7)	N1-Li1-N2 (x3)	75.0(8)
N1-Li1-N2 (x6)	133.46(24)	N1-Li1-N2 (x6)	132.95(29)
N2-Li1-N2 (x3)	82.5(7)	N2-Li1-N2 (x3)	82.6(7)

Table 4-8: Bond lengths and angles adapted from ref. 18.

Vector	Length (Å)	Vector	Length (Å)
Mo1-Nl (x3)	2.095 (4)	Lil-Nl (x3)	2.179 (18)
Mol-N2 (x3)	2.091 (4)	Lil-N2 (x3)	2.098 (17)
Angle	**Degrees**	**Angle**	**Degrees**
N1-Mo1-N1 (x6)	86.34 (9)	N1-Li1-N2 (x3)	177.3 (9)
N1-Mo1-N2 (x3)	75.45 (9)	N1-Li1-N2 (x6)	95.72 (8)
N1-Mo1-N2 (x6)	133.41 (3)	N2-Li1-N2 (x3)	86.2 (9)
N1-Li1-N1 (x3)	82.3 (8)		

The morphology of lithium molybdenum nitride, when analysed by SEM, was seen to be very different in places to that of the molybdate precursor, the surface of the particles were covered in lots of small scale particulates (Figure 4-4 and Figure 4-5). The large particles are expected to be some molybdate that has not been reacted with the NH$_3$ during the ammonolysis (c.f. Figure 3-7) [This cannot be confirmed due to technical difficulties with the EDX at the time of measurement].
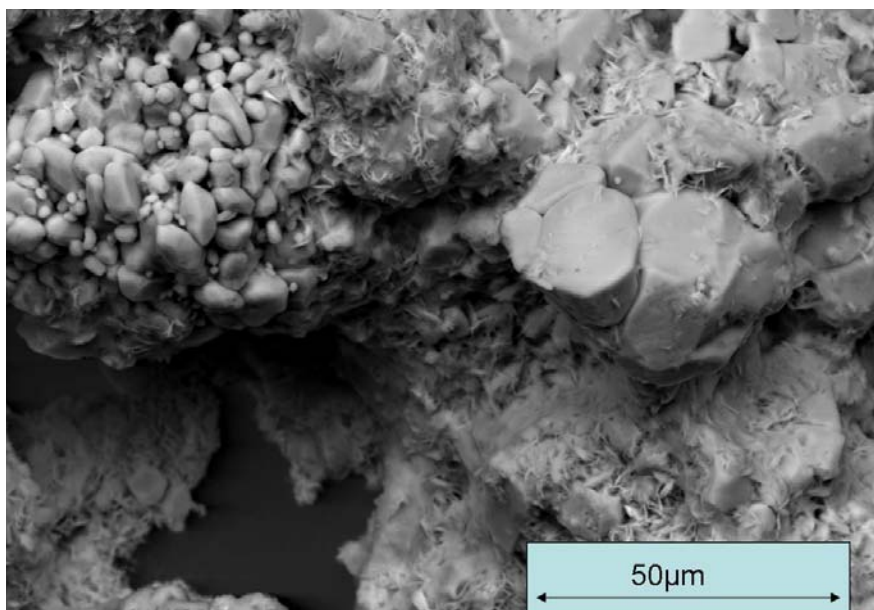
Figure 4-4: SEM image of LiMoN$_2$ (Sample 5).
Sample prepared via the high temperature synthetic route.
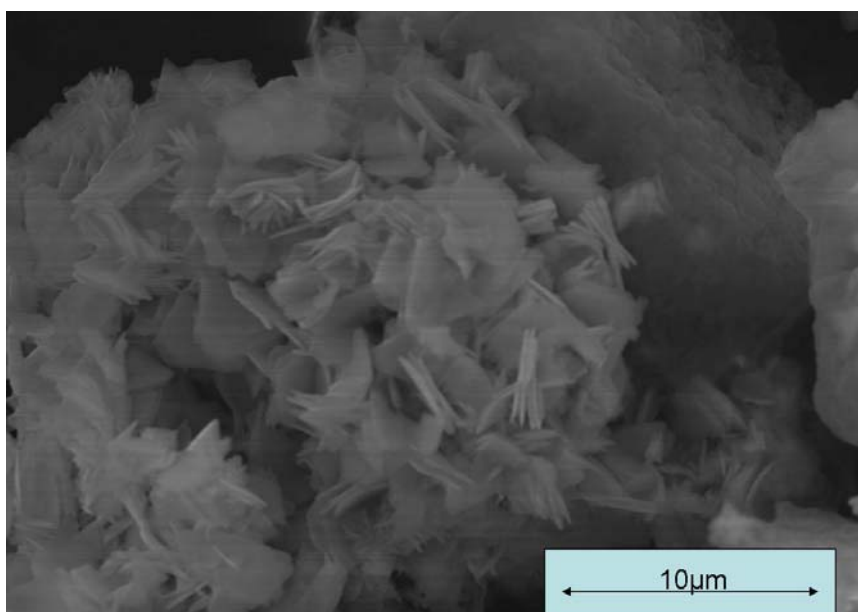
Figure 4-5: SEM image of LiMoN$_2$ (Sample 8).
Sample prepared via the high temperature synthetic route.

The appearance of small scale particulates only occurs after the ammonation process and none of these are seen prior to the exposure of the molybdate to a flow of ammonia. The process has the same effect on the molybdates synthesized at room temperature as shown in Figure 4-6 and Figure 4-7.
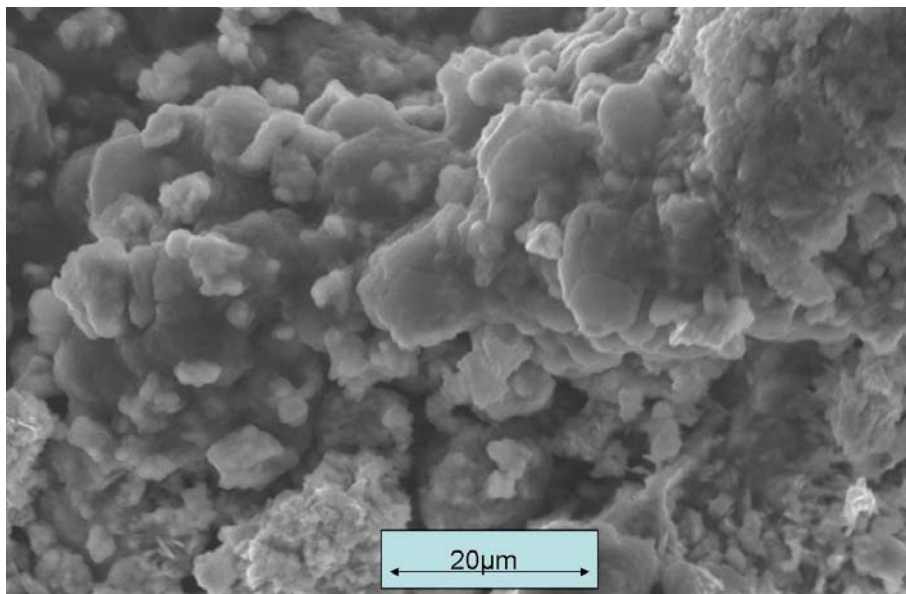
Figure 4-6: SEM image of LiMoN$_2$ (Sample 12).
Sample prepared via the room temperature synthetic route.
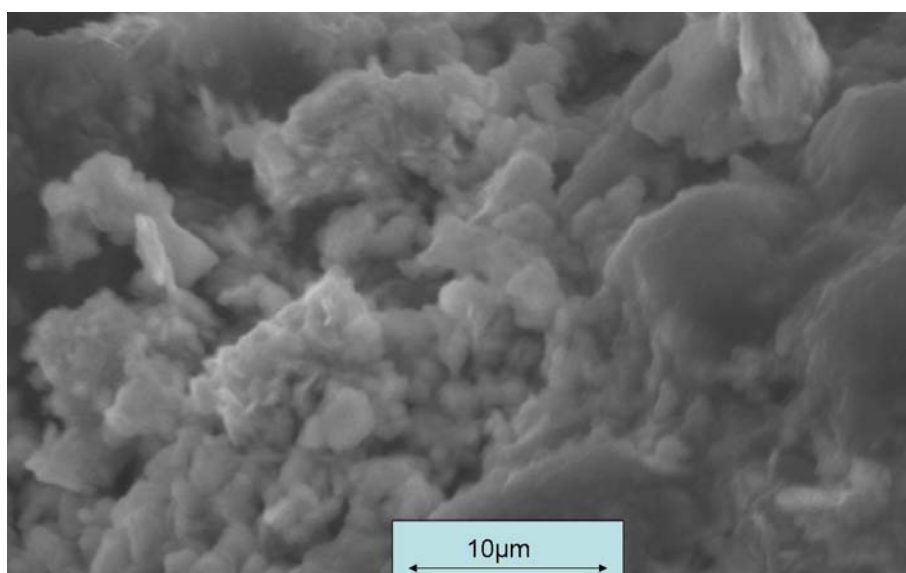
Figure 4-7: SEM image of LiMoN$_2$ (Sample 12).
Sample prepared via the room temperature synthetic route.

The formation of small scale 'plates' can be attributed to the formation of the nitride, although this cannot be verified by EDX as this shows that there is oxygen present in the sample with a 1:1:1 ratio of Mo:N:O suggesting the formation of an oxynitride or confirming the presence of Li$_2$O and Li$_2$MoO$_4$ along with LiMoN$_2$ as seen by XRD.

The formation of the nitride though reaction with ammonia gas at 700°C in an alumina boat was very different to the result of the process used by Aika[41] and

McKay[46] in which the sample was held in a silica tube between two silica wool plugs and then ammonia passed through the sample.

The resultant pattern acquired from X-ray diffraction (as seen in Figure 4-8) shows pure phase lithium molybdenum nitride with none of the residual lithium molybdate peaks seen in the previous reactions conducted in the alumina boat.
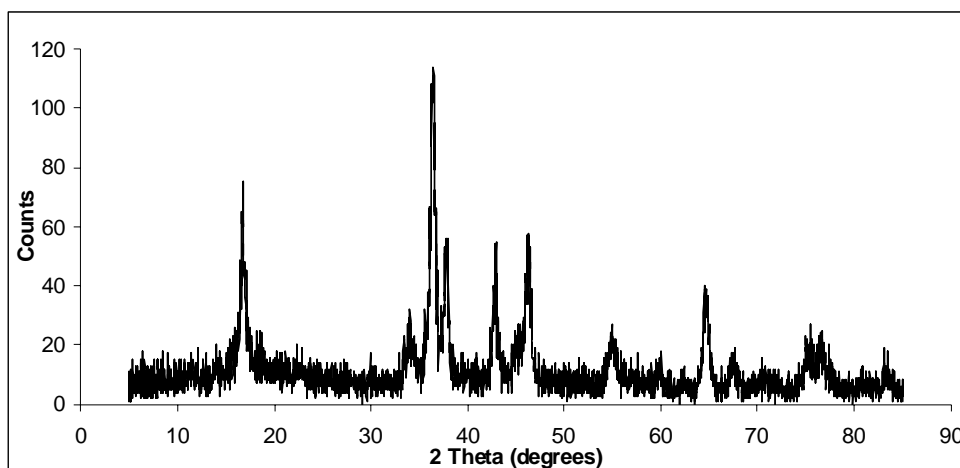
Figure 4-8: XRD pattern of Sample 11.

A Rietveld refinement was carried out and the resultant pattern was indeed the lithium molybdenum nitride along with trace amounts of lithia (which could form from the reaction of any excess lithium on exposure to the air or moisture when the sample is discharged from the reactor). The observed difference plot and related data is shown in Figure 4-9 and Table 4-9.

Figure 4-9: Final profile fit obtained from the X-ray diffraction data for $LiMoN_2$ (Sample 11). The observed data are crosses, the calculated profile the solid line and the lower continuous line the difference plot. Tick marks show allowed reflection positions.

Table 4-9: Sample 11 Refined parameters.
χ^2 =1.825 (25 Variables), R_{wp} (%) = 16.01, R_p (%) = 12.60;
‡ - Parameters fixed
Lithium Molybdenum nitride; R3m, $a = b$ = 2.8776(8) Å, c = 15.741(4) Å.

Atoms	x	y	z	Occupancy	100x U_{iso} /U_{eq} (Å^2)
Li 1	0.0	0.0	-0.04235(9)	0.85‡	1.96(14)
Mo 1	0.0	0.0	-0.04235(9)	0.15‡	1.96(14)
Li 2	0.0	0.0	0.7849(10)	0.15‡	2.00‡
Mo 2	0.0	0.0	0.7849(10)	0.85‡	2.00‡
N 1	0.0	0.0	0.1793(14)	1‡	2.4(5)
N 2	0.0	0.0	0.3286(14)	1‡	2.4(5)
Lithia: Fm-3m, a = b = c = 4.6463(28) Å					
Li 1	0.2500	0.2500	0.2500	1‡	2.50‡
O 1	0.0	0.0	0.0	1‡	2.50‡

The 'clean' pattern formed from the reaction in the plug-flow regime shows how the effect of the flow of ammonia through the sample rather than over it affects the nitride. The plug flow regime is seen to fully nitride the samples and leave no oxide phases in the bulk nitride as seen in the regime in which an alumina boat is used.

Further syntheses were carried out using a 25% N_2/H_2 feed gas to see if the reaction could be conducted under this feed gas mixture. This has some background in work conducted by McKay in which Co_3Mo_3N can be partially synthesised using this as opposed to NH_3 gas.
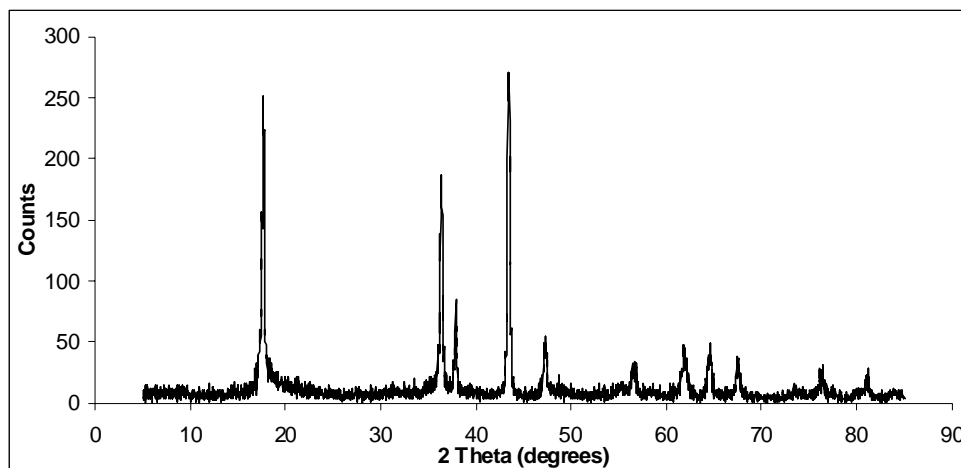
Figure 4-10: XRD pattern of Sample 13.

The pattern shown in Figure 4-10 is that of Li_2MoO_3 indicating that the molybdate is transformed from Li_2MoO_4 to Li_2MoO_3. This reaction is not seen under NH_3, but is a pure phase product as seen by the XRD pattern. Refinements were undertaken and the results are shown in Figure 4-11 and Table 4-10.
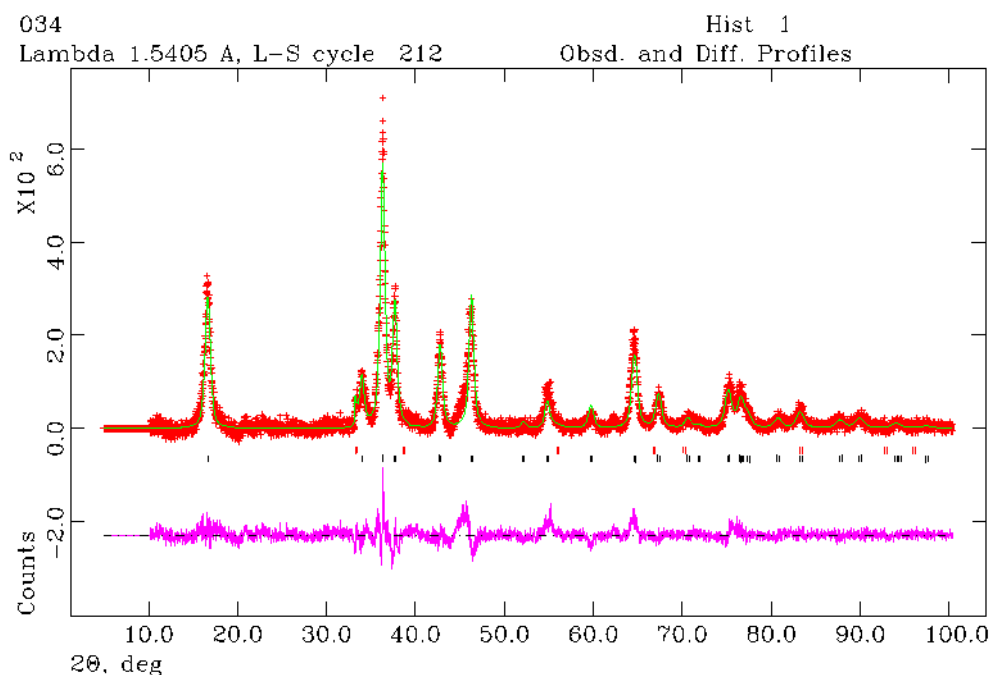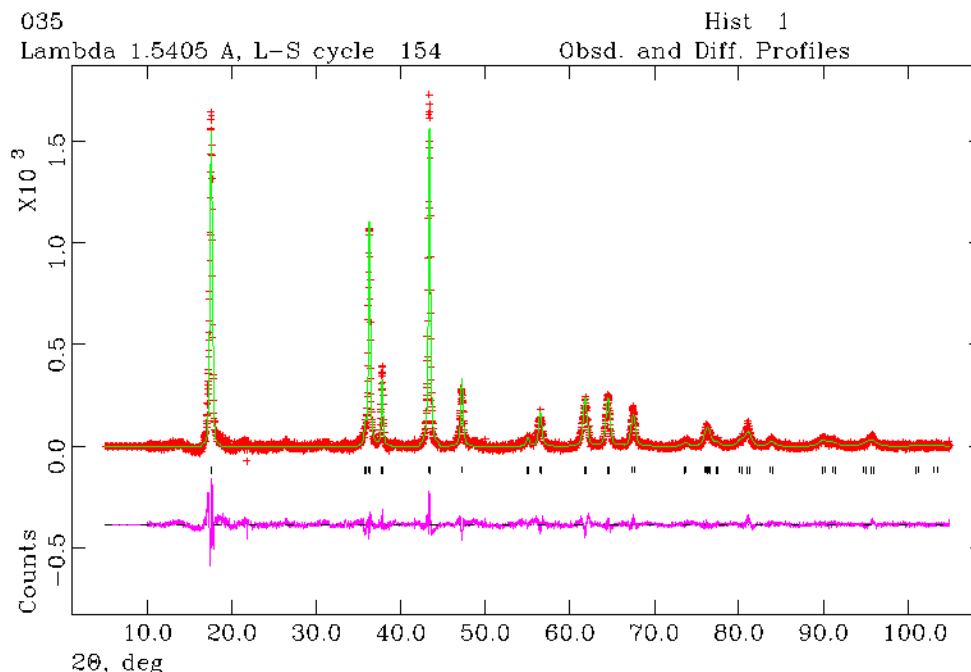

Figure 4-11: Final profile fit obtained from the X-ray diffraction data for Sample 13.
The observed data are crosses, the calculated profile the solid line and the lower continuous line the difference plot. Tick marks show allowed reflection positions.

Table 4-10: Sample 13 Refined parameters.
χ^2 =2.069 (40 Variables), R_{wp} (%) = 16.24, R_p (%) = 12.62;
‡ - Parameters fixed
Lithium Molybdenum oxide; R-3m, $a = b$ = 2.8791(5) Å, c = 14.9524(22) Å.

Atoms	x	y	z	Occupancy	100x U_{iso} /U_{eq} ($Å^2$)
Mo 1	0.0	0.0	0.50	0.385(14)	1.794(8)
Li 1	0.0	0.0	0.50	0.615(14)	1.794(8)
Li 2	0.0	0.0	0.0	1.0‡	1.75‡
O 1	0.0	0.0	0.24737(34)	1.0‡	1.37(4)

The presence of only lithium molybdate (Li_2MoO_3) shows how the reaction feed gas of 25 % N_2/H_2 has no nitridation capability towards Li_2MoO_4 under the conditions applied and thus apparently only reduces the molybdate.

4.4 Summary

The formation of a very crystalline nitride with few or no impurities present was found to be very problematic. The nitrides formed all appeared to have poorly crystalline character with a suggestion of amorphous components when analysed by X-ray diffraction. Many of the samples still had remnants of the starting molybdate present and also significant quantities of lithia which is expected from the reaction scheme.

The nitrides formed via a plug-flow regime were found to only contain the nitride and lithia with no molybdate trace found. This regime allowed for the ammonia to pass through the sample and for the whole sample to be exposed to the gas as opposed to the method primarily employed using a silica boat in which the gas is passed over the surface of the sample, eliminating potential 'by-pass' effects.

The possibility for incomplete nitridation while employing the boat method is highly likely as the sample is only exposed to the gas on the surface and relies on diffusion between the particles. This would explain the large quantities of the molybdate present in the sample when analysed by X-ray diffraction. This is further enforced by the SEM which shows small plate like particles on the surface of the oxide particles (i.e. an oxide core). EDX confirms the presence of oxygen in the samples. This could, as previously stated, be due to the molybdate being incompletely nitrided although it could also be due to the formation of an

oxynitride. These have been seen previously for molybdenum nitrides[48]. This possibility is hard to confirm as any possible oxynitride structure is not known and X-rays cannot distinguish between O^{2-} and N^{3-}.

The possibility of the oxynitrides would also explain the sub-stoichiometric quantities of nitrogen found in the samples when analysed. The presence of the oxynitride could account for the low nitrogen content as could mixtures of the oxides and (oxy)-nitrides.

The surface area of the samples is low with an average area of ca. $4m^2g^{-1}$. This is about the same as the molybdate precursor although presence of the small scales 'plates' on the surface could have been expected to increase the surface area.

When the molybdate precursor was reacted with 25% N_2/H_2, the sample was reduced to Li_2MoO_3. This is not as expected as for the synthesis of Mo_2N from the direct reaction of MoO_3 with 25% N_2/H_2. However the presence of Li_2MoO_3 is consistent more with the heating of the molybdate as previously seen in the variable temperature XRD shown in Figure 3-12.

5　Ammonia Synthesis Testing

5.1　Introduction

The use of molybdenum containing nitrides for ammonia synthesis has been widely researched previously and many possible catalysts have been discovered. Binary molybdenum nitrides have been long known for their ammonia synthesis efficacy[41,42,43,44].The best of the nitrides reported to date are cobalt molybdenum nitride and caesium promoted cobalt molybdenum nitride (as discussed previously in Section 1.1.3)[45,47,48]. For ease of comparison with the literature, the reactions using lithium molybdenum nitrides described in this section were carried out under comparable conditions to those applied by Aika and co-workers[43,63] who studied Co_3Mo_3N and Cs^+/Co_3Mo_3N.

Generally nitrides have a relatively high activity for ammonia synthesis and the possible role of the 'lattice' nitrogen in the system can be questioned. It is possible that a Mars van Krevelen like mechanism, in which the 'lattice' nitrogen itself is active, could occur.

The role of 'lattice' nitrogen in Co_3Mo_3N has now been investigated further with the formation of a new η-12 phase Co_6Mo_6N[46] by hydrogenation with 25% Ar/H_2 at high temperatures being reported. During denitridation it was the 'lattice' nitrogen which provided the source of nitrogen for the synthesis of the ammonia observed. Therefore, as described in this section, additional M-Mo-N systems have been studied to investigate if this process is seen in other systems.

5.2　Experimental

The samples were all tested at ambient pressure for their potential as ammonia synthesis catalysts. The method employed used a fixed bed reactor over which reactant gas ($60mlmin^{-1}$) of either 25% N_2/H_2 or 25% Ar/H_2 was flowed. The production of ammonia was measured by the change in conductivity of 200ml 0.00108 $molL^{-1}$of sulfuric acid, a procedure adopted by Aika and co-workers[41,43].

The reaction conditions were kept constant with a fixed amount of sample (0.4g) and an initial pre-treatment stage in which the sample was exposed to 25% N_2/H_2 gas for 2 hours at 700°C, which removed any surface oxide layers present . The reactor was then cooled to 400°C, the appropriate reaction gas was selected and the conductivity measurements started. In the reactions conducted under 25% Ar/H_2 the temperature was increased at different stages throughout the reaction to monitor the production of ammonia as a function of temperature.

The samples were tested under either a 25% N_2/H_2 gas mixture or a 25% Ar/H_2 gas mixture. The 25% N_2/H_2 mix allows for the samples to be tested for their ability to form ammonia with an external source of nitrogen. The 25% Ar/H_2 mix demonstrates the ability of the sample to produce ammonia with the only source of available nitrogen being that present in the nitride itself. Thus the reactivity of the 'lattice' nitrogen can be assessed.

The samples examined were all subject to elemental analysis both before and after reaction to determine the effects of the different reactant gases. This was used to observe the extent to which the 'lattice' nitrogen is active in the samples, as any change in the percentage of nitrogen can be linked to the activity of the nitrogen.

5.3   Results and Discussion

5.3.1   25%/75% N_2/H_2 feed gas reactions

The reactions using 25% N_2/H_2, were run for 5½ hours at 400°C after an initial pre-treatment stage at 700°C for 2 hours under 25% N_2/H_2. This removed any surface oxide which may have formed on discharge to air after ammonolysis. The samples exhibited similar reaction profiles. There was a relatively sharp initial drop in conductivity over the first 30 to 60 minutes, then a plateauing of the change in concentration of the acid solution. This can be clearly seen in Figure 5-1 and Figure 5-2.
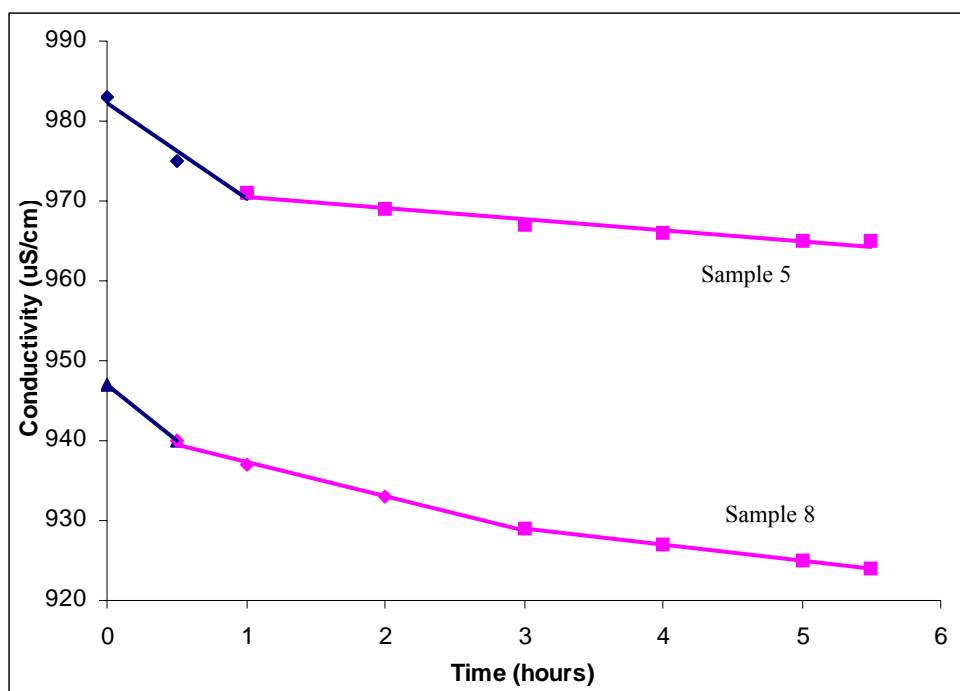
Figure 5-1: Reaction profile for samples 5 and 8 at 400°C under 25% N_2/H_2.
The blue line indicates the initial conductivity decrease; the magenta line represents the subsequent plateau effect.
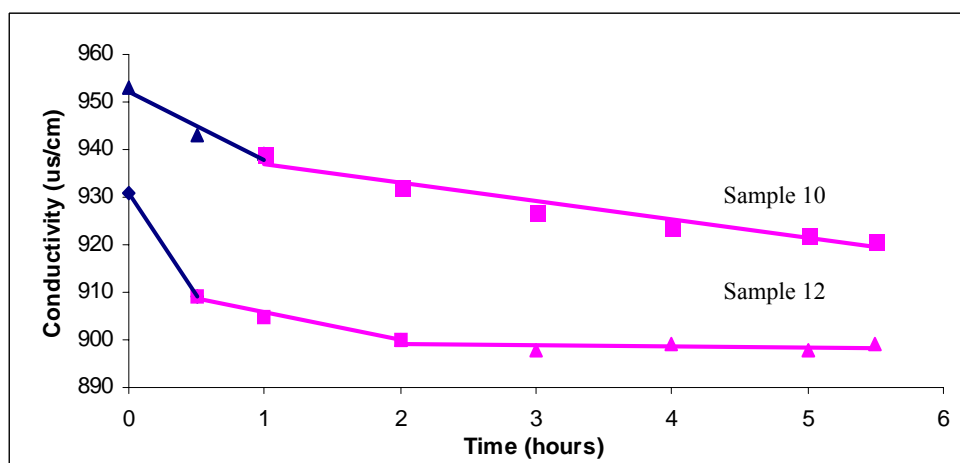
Figure 5-2: Reaction profiles for samples 10 and 12 at 400°C under 25% N_2/H_2.
The blue line indicates the initial conductivity decrease; the magenta line represents the subsequent plateau effect.

The profile is similar for nitrides prepared using both types of precursor, i.e. those synthesised at room temperature and those synthesised at high temperature. This profile can potentially be attributed to surface NH_x species, remaining from the initial pre-treatment stage of the reaction, being hydrogenated in the first 60 minutes, after which a steady state rate of NH_3 production occurs. The possibility of surface NH_x species has been reported in previous work carried out on molybdenum nitride, suggesting that the species adsorb on the surface of the

nitride during preparation and/or pre-treatment and then desorb during reaction[64,65].

The ratio of the rates of reaction for the samples between the relatively large initial decrease and the plateau is around an order of magnitude. Table 5-1 shows the rates of reaction, calculated from the change in conductivity in the sulfuric acid solution.

Table 5-1: Rates of reaction for samples reacted under 25% N_2/H_2 feed gas.

Sample	Rate of Reaction ($molh^{-1}g^{-1}$)		
	Initial	Plateau	
1	3.650×10^{-5}	6.722×10^{-6}	
2	1.460×10^{-5}	5.628×10^{-6}	
5	2.920×10^{-5}	5.831×10^{-6}	
8	2.190×10^{-5}	6.810×10^{-6}	3.650×10^{-6}
10	2.555×10^{-5}	6.990×10^{-6}	
12	8.030×10^{-5}	1.069×10^{-5}	4.674×10^{-7}

After reaction, the samples were analysed by X-ray diffraction as seen in Figure 5-3 and Figure 5-4. This allowed a comparison to be made between the samples before and after the reaction and any changes that had occurred to the structure to be identified.
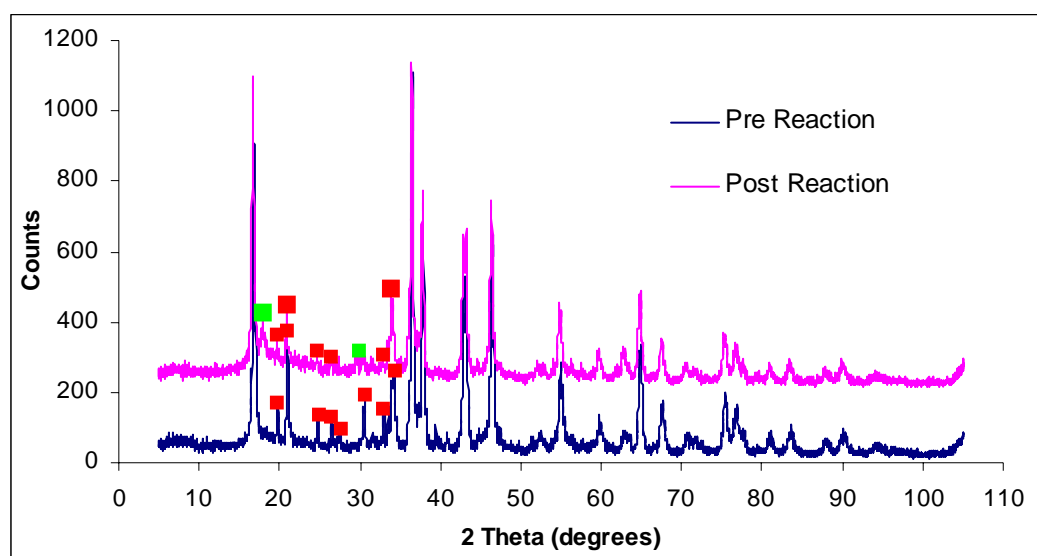
Figure 5-3: XRD patterns showing differences before and after reaction for Sample 8 with 25% N_2/H_2 feed gas.
Red = Li_2MoO_4, Green = Li_2MoO_3
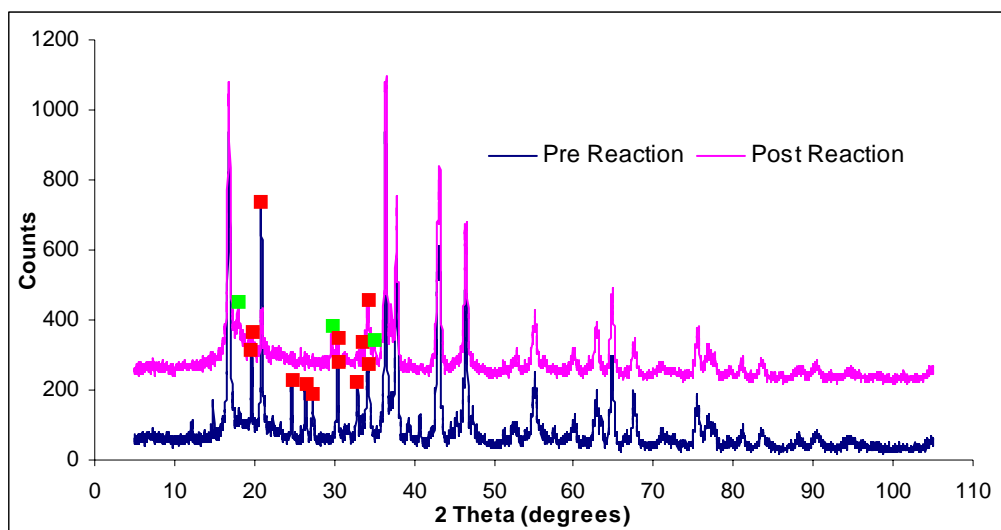
Figure 5-4: XRD patterns showing differences before and after reaction for Sample 10 with 25% N_2/H_2 feed gas.
Red = Li_2MoO_4, Green = Li_2MoO_3

The XRD patterns still show the main phase to be the $LiMoN_2$. The main changes seen in the patterns relate to a reduction in the relative intensity of the lithium molybdate (Li_2MoO_4) reflections and an increase in the reflections related to that of lithium (IV) molybdate (Li_2MoO_3). The formation of these reflections and the loss of the Li_2MoO_4 reflections can be correlated with an experiment performed on the precursor lithium molybdate, where Li_2MoO_4 was entirely converted to Li_2MoO_3 under flowing 25% N_2/H_2 gas (Section 3.3).

Table 5-2: Elemental compositions of samples.

Sample	Elemental composition (Nitrogen wt %)		Loading of N in Lithium molybdenum nitride*	Assumed Stoichiometry Post (N_2/H_2)
	Pre Reaction	Post (N_2/H_2)		
2	9.81	9.45	57%	"$LiMoN_{1.13}$"
5	12.54	10.91	66%	"$LiMoN_{1.32}$"
8	11.52	9.33	56%	"$LiMoN_{1.13}$"
10	10.58	7.94	48%	"$LiMoN_{0.96}$"
12	9.00	6.45	39%	"$LiMoN_{0.78}$"

* Loadings calculated from the weight % of nitrogen present in the sample.
N.B.: Loadings and stoichiometry based on the presence of $LiMoN_2$ and Li_2O.

From the elemental analysis, it is possible to calculate the assumed stoichiometry of the samples, which is shown to be reduced upon reaction as shown in Table 5-3. This illustrates that the samples are more nitrogen deficient after reaction with 25% N_2/H_2, which could be attributed to the loss of surface NH_x species upon reaction.

Table 5-3: Assumed stoichiometries of samples.

Sample	Assumed Stoichiometry	
	Pre Reaction	Post (N_2/H_2)
2	"$LiMoN_{1.18}$"	"$LiMoN_{1.13}$"
5	"$LiMoN_{1.5}$"	"$LiMoN_{1.32}$"
8	"$LiMoN_{1.38}$"	"$LiMoN_{1.13}$"
10	"$LiMoN_{1.26}$"	"$LiMoN_{0.96}$"
12	"$LiMoN_{1.08}$"	"$LiMoN_{0.78}$"

N.B.: Stoichiometry based on the presence of $LiMoN_2$ and Li_2O.

The calculations used to determine the stoichiometries, rely on the presence of lithium nitride and lithia only, therefore excluding the possibility of starting material remaining in the sample.

5.3.2   25%/75% Ar/H₂ feed gas reactions

The samples were initially treated with 25% N_2/H_2 for two hours at 700°C which removes any surface oxide from the sample prior to the reaction. After pre-treatment, the temperature was lowered to 400°C and the feed gas changed to 25% Ar/H_2. As with 25% N_2/H_2, the samples all showed an initial relatively sharp decrease in conductivity followed by a plateau at 400°C and then after, the temperature increase to 500°C, the conductivity decreased again and likewise after further temperature rises to 600°C and 700°C.

This is clearly shown in Figure 5-5 in which the profile has been split into the different temperature ranges.

Figure 5-5: Reaction profile of Sample 5 under 25% Ar/H₂.
Magenta line = 400°C, Orange line = 500°C, Purple line = 600°C and Green line = 700°C.

The profile clearly shows the initial decrease in conductivity in the first 30 to 60 minutes followed by the plateau effect, then after the temperature is increased to 500°C the conductivity decrease is more rapid. After a further increase in temperature to 600°C and then 700°C the decrease in conductivity shows a large initial drop followed by a slowing in the rate. However the rate doesn't level off, as was observed at lower temperatures.
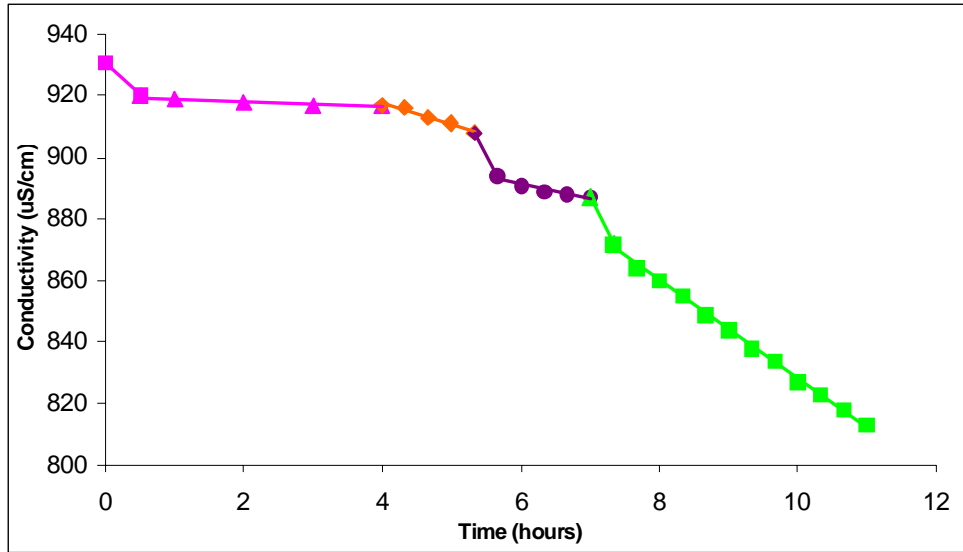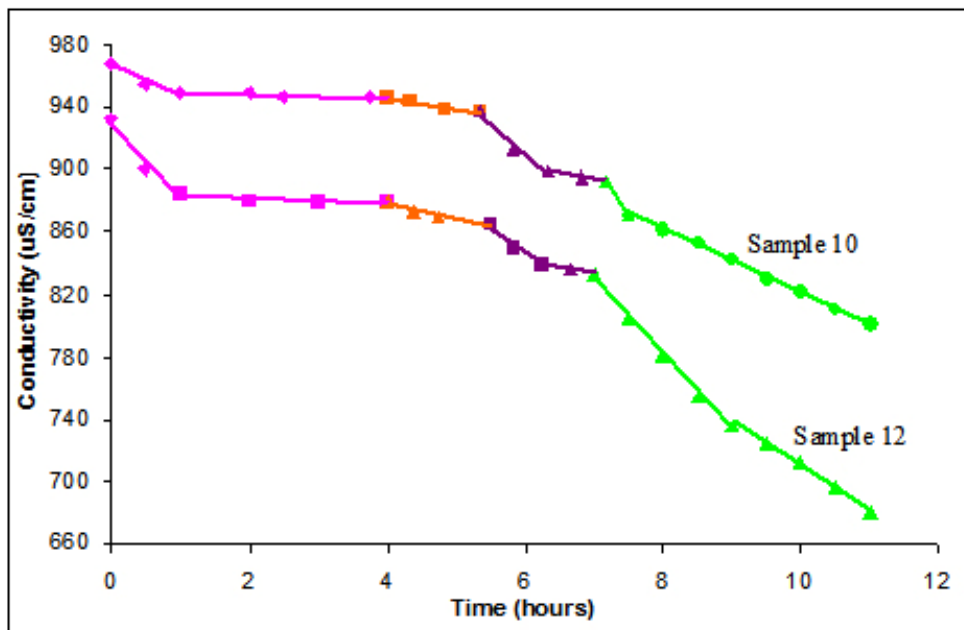

Figure 5-6: Reaction profile of Samples 10 and 12 under 25% Ar/H₂.
Magenta line = 400°C, Orange line = 500°C, Purple line = 600°C and Green line = 700°C.

The samples synthesised at different temperatures all showed similar profiles as shown in Figure 5-5 and Figure 5-6. The main area of difference is at 700°C which shows differences in the profiles depending on the sample. Table 5-4 shows that the rates of reactions for the samples are fairly consistent across the samples with no major differences in the rates depending on the method of synthesis.

Table 5-4: Rates of reactions for samples undergoing ammonia synthesis testing with 25% Ar/H_2 feed gas.

	Sample	Temperature (°C)			
		400	500	600	700
Rate of Reaction $(molh^{-1}g^{-1})$	3	1.679×10^{-4} 1.115×10^{-5}	9.308×10^{-6}	9.855×10^{-5} 2.972×10^{-5}	1.259×10^{-4} 3.891×10^{-5}
	5	4.015×10^{-5} 1.580×10^{-6}	1.259×10^{-5}	7.665×10^{-5} 9.308×10^{-6}	8.213×10^{-5} 2.896×10^{-5}
	10	3.650×10^{-5} 2.404×10^{-6}	1.296×10^{-5}	6.935×10^{-5} 1.527×10^{-5}	1.150×10^{-4} 3.680×10^{-5}
	12	8.760×10^{-5} 2.920×10^{-6}	1.729×10^{-5}	6.014×10^{-5} 1.705×10^{-5}	8.906×10^{-5} 5.110×10^{-5}

The temperatures have different values relating to the different stages of the reaction process (some areas have two rates relating to the initial decrease or plateau stage).

The reactions are seen to be very temperature dependent and increasing the temperature at which the reaction is conducted increases the amount of ammonia produced. With no nitrogen present in the feed gas the sample produces ammonia with the nitrogen present in the sample and this means that the total amount of ammonia which can be produced is limited.

Table 5-5: Elemental compositions of samples

Sample	Elemental composition (Nitrogen wt %)		Loading of N in Lithium molybdenum nitride*	Assumed Stoichiometry
	Pre Reaction	Post (Ar/H_2)		
3	13.04	7.59	46%	"$LiMoN_{0.92}$"
5	12.54	10.44	63%	"$LiMoN_{1.26}$"
10	10.58	6.61	40%	"$LiMoN_{0.80}$"
12	9.00	5.61	34%	"$LiMoN_{0.68}$"

* Loadings calculated from the weight % of nitrogen present in the sample.
N.B.: Loadings and stoichiometry based on the presence of $LiMoN_2$ and Li_2O.

The elemental composition shows that the samples have lost a considerable amount of nitrogen as shown in Table 5-5. However this is not reflected in the post-reaction XRD studies as the "lithium molybdenum nitride" phase is still observed after reaction and the position of the reflections remain unshifted. The weight percentage of nitrogen from elemental analysis can be used to calculate the assumed stoichiometry of the samples post-reaction. Table 5-6 shows the substantial differences between the samples pre- and post-reaction, as expected.

Table 5-6: Assumed stoichiometry of samples.

Sample	Assumed Stoichiometry	
	Pre Reaction	Post (Ar/H$_2$)
3	"LiMoN$_{1.56}$"	"LiMoN$_{0.92}$"
5	"LiMoN$_{1.5}$"	"LiMoN$_{1.26}$"
10	"LiMoN$_{1.26}$"	"LiMoN$_{0.80}$"
12	"LiMoN$_{1.08}$"	"LiMoN$_{0.68}$"

Therefore another source of nitrogen must be present in the reaction that cannot be seen within the XRD pattern. Either it is obscured by other reflections or else it is contained within the amorphous background.

5.3.3 Lithium Nitride Reactions

With lithia being an impurity present in the reaction, lithium is present in a slight excess during the reaction. This could be converted by reaction with ammonia or 25% N$_2$/H$_2$ to, for example, lithium nitride. Accordingly such lithium nitride samples have been examined.

Ammonia synthesis reactions with both 25% N$_2$/H$_2$ and 25% Ar/H$_2$ were conducted so that a direct comparison could be drawn between the lithium molybdenum nitride and the lithium nitride samples.

0.4g of Li_3N (Alfa Aesar) was exposed to air for an hour prior to the reaction. This, as with the lithium molybdenum nitride, would be expected to react with air and form oxides and, in the case of lithium nitride, amides and imides. The sample was initially treated for two hours under 25% N_2/H_2 gas at 700°C. The temperature was then reduced to 400°C and followed as described previously by the change in conductivity of sulfuric acid.

The reaction demonstrated that the sample was able to produce ammonia at 400°C for a longer period of time than that possible in the lithium molybdenum nitride samples. This prolonged production of ammonia can be clearly seen in Figure 5-7 in which the conductivity decrease is rapid and constant throughout the reaction. The general form of the profile differs from those reported in this chapter. The comparatively large initial decrease followed by plateau as seen in the reaction with lithium molybdenum nitride was not observed.
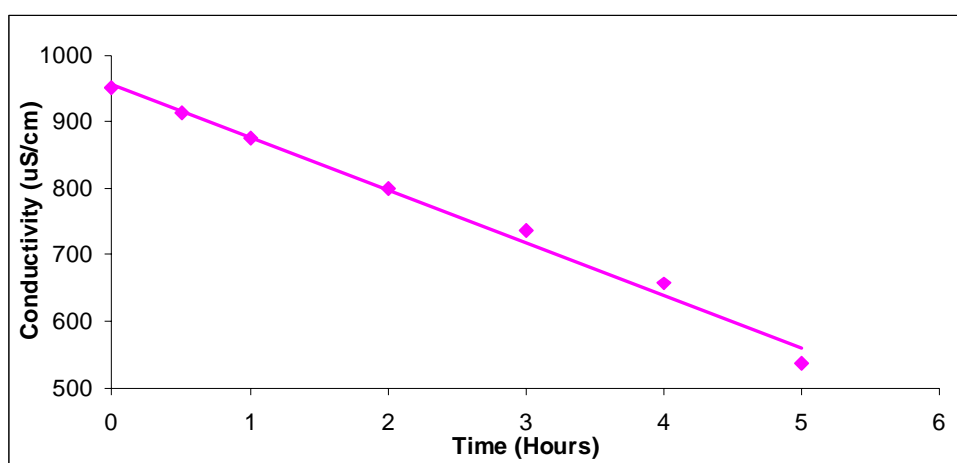
Figure 5-7: Reaction profile of lithium nitride under 25% N_2/H_2 at 400°C.

The constant ammonia production rate for lithium nitride is considerably higher than the rate for lithium molybdenum nitride. The rate of 1.445 x10^{-4} molhr^{-1}g^{-1} for the lithium nitride is comparable to that of the lithium molybdenum nitride at 700°C under 25% Ar/H_2 and is close to the mass normalised activity (6.60 x10^{-4} molhr^{-1}g^{-1}) for Co_3Mo_3N reported by Aika and co-workers[43,66]. The XRD patterns (Figure 5-8) show that the pre- and post-reaction samples are very different and show how the sample changes from the combination of α- and β-lithium nitride, amide, and hydroxide to lithium imide, oxide and hydride after reaction.

The presence of the hydroxide and amide prior to reaction is expected due to the exposure to air, presence of imide, oxide and hydride after reaction can be attributed to the exposure of the sample to air post reaction and also possibly to moisture content of the gases used in the reaction.

Figure 5-8: XRD patterns of the sample pre and post reaction.
Magenta pattern = pre reaction, blue line = post reaction 25% N_2/H_2.
Pale blue = LiOH, Green = Li_3N, Magenta = $LiNH_2$, Orange = Li_2NH, Red = LiH, Dark Blue = Li_2O.

The reaction with 25% Ar/H_2 feed gas produces ammonia at 400°C for a considerable amount of time at a constant rate of production. The rate is once again comparable with the lithium molybdenum nitride at 700°C but will continue producing ammonia for some hours as shown in Figure 5-9.
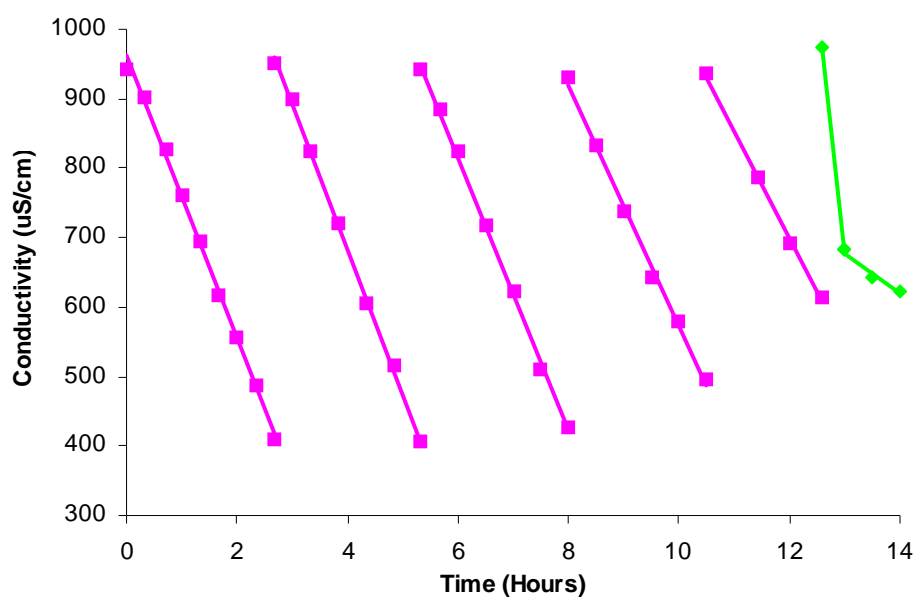
Figure 5-9: Reaction profile of lithium nitride under 25% Ar/H_2.
Magenta Lines = 400°C, Green Line = 700°C
N.B. Different flasks of acid were needed to follow the reaction hence the different traces.

The rate of the reaction was constant at 400°C for up to 13 hours at which time the temperature was increased to 700°C, after which point the reaction appeared to end. This sudden cessation in the reaction could be due to the complete decomposition of lithium nitride at high temperatures.

The rate of reaction (shown in Table 5-7) for the different traces illustrates how the reaction proceeds with the rate remaining fairly constant at 400°C, averaging 3.525×10^{-4} molhr^{-1}g^{-1}, and increasing when the temperature was increased to 700°C. This rate is almost three times as fast as the rate for the lithium nitride under 25% N$_2$/H$_2$ (1.445×10^{-4} molhr^{-1}g^{-1}); however the exposure to air prior to reaction may have been different causing this difference in the rates of reaction for the two gas regimes.

Table 5-7: Rates of reaction for reaction of lithium nitride with 25% Ar/H$_2$.

	Li$_3$N (Figure 5-9)	
	400°C	**700°C**
Rate of Reaction (molhr^{-1}g^{-1})	3.728×10^{-4}	
	3.784×10^{-4}	1.275×10^{-3}
	3.596×10^{-4}	1.059×10^{-4}
	3.159×10^{-4}	
	2.832×10^{-4}	

The XRD patterns show how the samples once again change from a mixture of the α- and β-Li$_3$N and the lithium amide and some hydroxide to the hydride and oxide and imide post-reaction. This is shown in Figure 5-10.
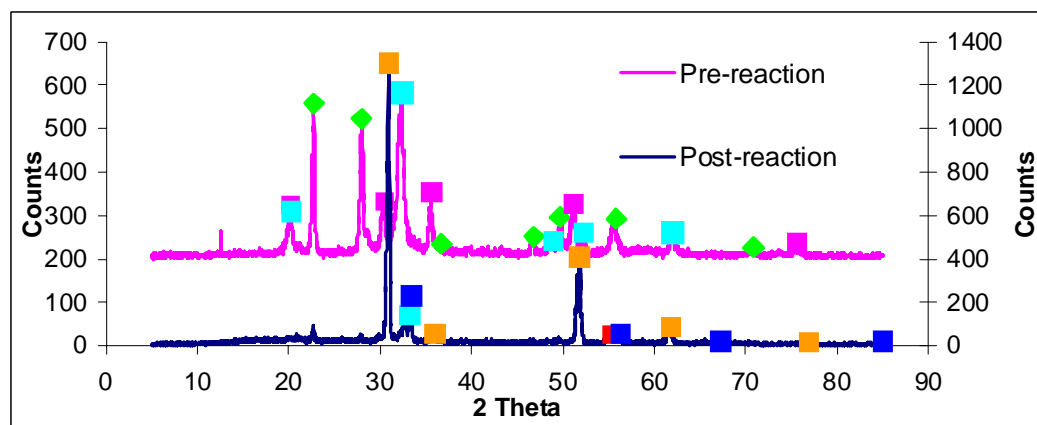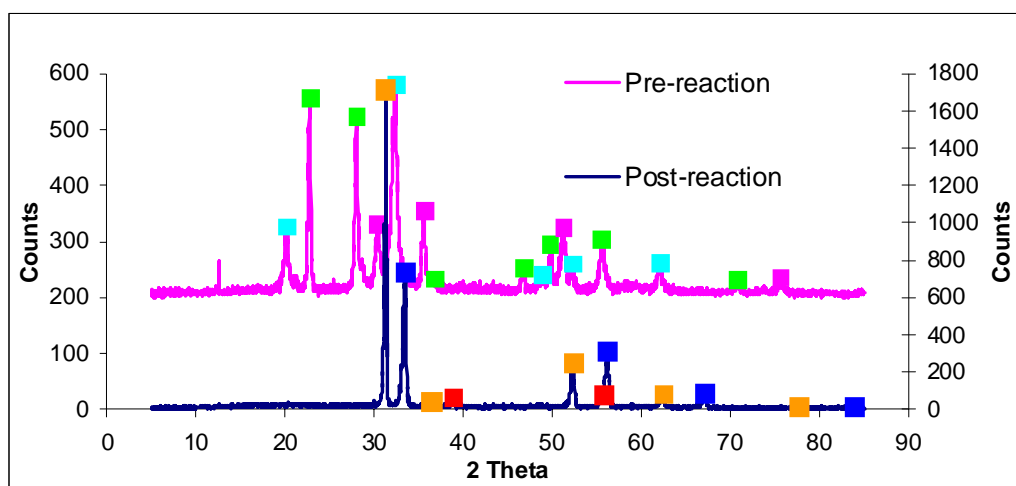
Figure 5-10: XRD patterns of the sample pre and post reaction.
Magenta pattern = pre reaction, blue line = post reaction 25% Ar/H_2.
Pale blue = LiOH, Green = Li_3N, Magenta = $LiNH_2$, Orange = Li_2NH, Red = LiH, Dark Blue = Li_2O.

The conversion to the imide and oxide is observed again in the post-reaction samples under (25% Ar/H_2). The reactions seem to be consistent with both feed gas regimes. The formation of the ammonia is therefore not dependent on the presence of nitrogen in the feed gases.

Therefore with the presence of $N_{2(g)}$ ruled out the role of $H_{2(g)}$ in the reaction was investigated. A reaction using pure $Ar_{(g)}$ was used with no initial pre-treatment under 25% N_2/H_2, thus avoiding any form involvement from either N_2 or H_2 gases in the reaction. The reaction followed the same heating regime – with an initial two hours at 700°C, before the temperature was reduced to 400°C and the rate of conductivity change was measured.

Figure 5-11 shows this profile under pure argon gas indicating a similar reaction profile to that indicated in Figure 5-7. The comparison of the rates of reaction under pure argon with the 25% Ar/H_2, shows how the rates at 400°C are comparable (1.108 $x10^{-4}$molhr^{-1}g^{-1} compared with 3.525x10^{-4} molhr^{-1}g^{-1} respectively). The comparisons between the rates can be seen in Table 5-8 and Table 5-9 and Table 5-10 at the end of this chapter.
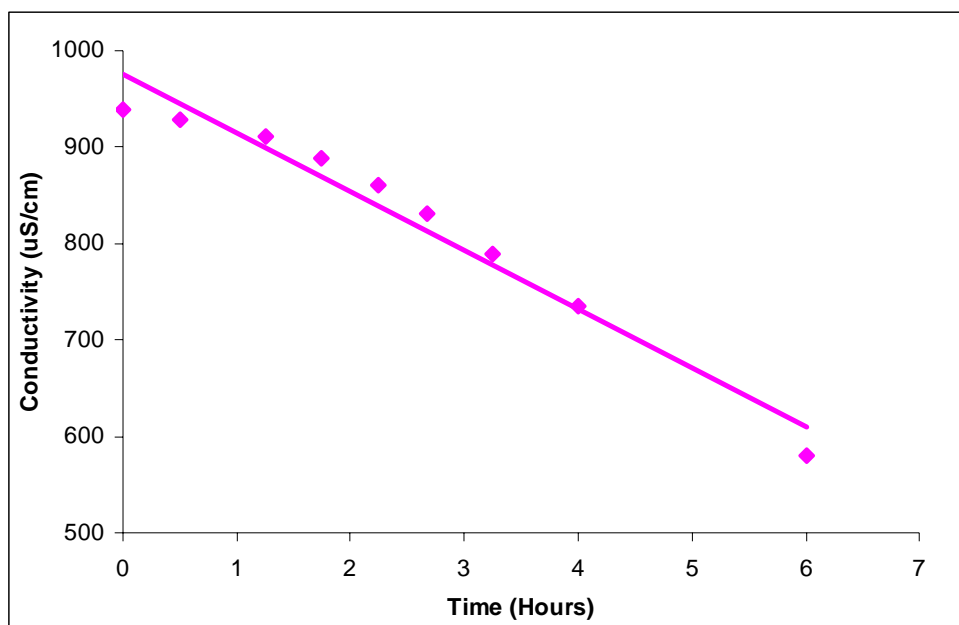
Figure 5-11: Reaction profile of Li₃N under Ar at 400°C.

The XRD pattern of the post reaction sample (Figure 5-12) was also similar with lithium hydride and oxide being present. This demonstrates that the process is analogous to the samples reacted under 25% Ar/H$_2$, thus assumed route of ammonia generation is through the decomposition of lithium amide. There is also the possibility that moisture in the feed gases and/or atmosphere causes the formation of lithium oxide during the reaction.

Figure 5-12: XRD pattern of post reaction Li₃N with Ar at 400°C.

Hu and Ruckenstein[67] had previously reported that in a reaction under He$_{(g)}$, lithium amide would form ammonia. This was shown to occur via the decomposition of the amide.

$$2LiNH_2 \rightarrow Li_2NH + NH_3$$

Table 5-8: Rates of reactions for samples undergoing ammonia synthesis testing with 25% N_2/H_2 feed gas.
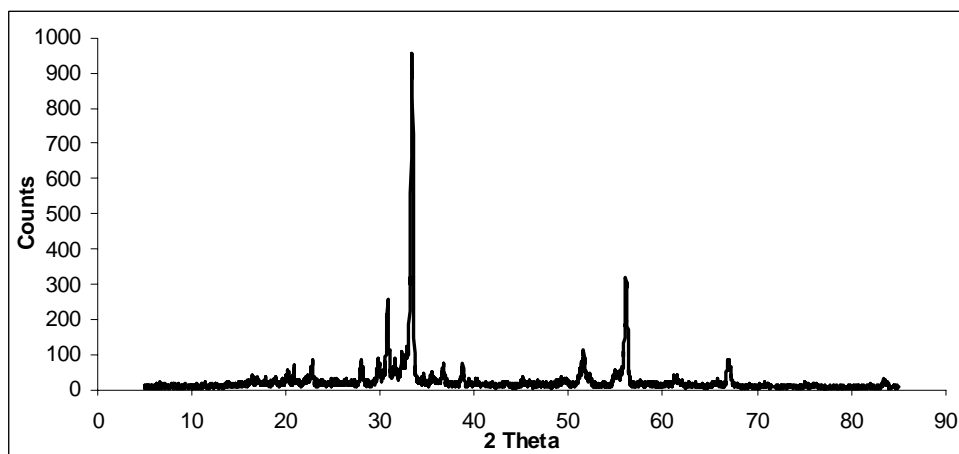
Sample	Rate of Reaction ($molh^{-1}g^{-1}$)	
	Initial	**Plateau**
1	3.650×10^{-5}	6.722×10^{-6}
2	1.460×10^{-5}	5.628×10^{-6}
5	2.920×10^{-5}	5.831×10^{-6}
8	2.190×10^{-5}	6.810×10^{-6} $\quad$ 3.650×10^{-6}
10	2.555×10^{-5}	6.990×10^{-6}
12	8.030×10^{-5}	1.069×10^{-5} $\quad$ 4.674×10^{-7}

Table 5-9: Rates of reactions for samples undergoing ammonia synthesis testing with 25% Ar/H_2 feed gas.

	Sample	Temperature (°C)			
		400	**500**	**600**	**700**
Rate of Reaction ($molh^{-1}g^{-1}$)	**3**	1.679×10^{-4} 1.115×10^{-5}	9.308×10^{-6}	9.855×10^{-5} 2.972×10^{-5}	1.259×10^{-4} 3.891×10^{-5}
	5	4.015×10^{-5} 1.580×10^{-6}	1.259×10^{-5}	7.665×10^{-5} 9.308×10^{-6}	8.213×10^{-5} 2.896×10^{-5}
	10	3.650×10^{-5} 2.404×10^{-6}	1.296×10^{-5}	6.935×10^{-5} 1.527×10^{-5}	1.150×10^{-4} 3.680×10^{-5}
	12	8.760×10^{-5} 2.920×10^{-6}	1.729×10^{-5}	6.014×10^{-5} 1.705×10^{-5}	8.906×10^{-5} 5.110×10^{-5}

Table 5-10: Rates of reaction for reaction of lithium nitride with 25% Ar/H_2.

	Li_3N (Figure 5-9)	
	400°C	**700°C**
Rate of Reaction ($molhr^{-1}g^{-1}$)	3.728×10^{-4} 3.784×10^{-4} 3.596×10^{-4} 3.159×10^{-4} 2.832×10^{-4}	1.275×10^{-3} 1.059×10^{-4}

6 Conclusion

The precursor, lithium molybdate (Li_2MoO_4), was shown to be relatively easily synthesised using two methods – a room temperature[51] and a high temperature[18] synthetic route. Both routes gave very pure samples of the R-3 polymorph, as confirmed by X-ray diffraction and scanning electron microscopy. The surface area of the samples was however very low with an average surface area of $5m^2g^{-1}$. Ammonolysis of the precursor has been shown to form nitrides with some impurities present.

The samples were tested as ammonia synthesis catalysts by reaction with 25% N_2/H_2 gas and 25% Ar/H_2 gas. The latter was used to determine the potential reactivity of lattice nitrogen. A relatively large amount of ammonia was produced in the first 30-60 minutes of reaction which was attributed to desorption of surface NH_x species. This was followed by a period of steady state reaction.

The reactions with 25% Ar/H_2 showed that the samples were active and would produce ammonia in the absence of nitrogen in the feed gas. Increasing the temperature highlighted that the rate of reaction is very temperature dependent.

Post-reaction X-ray diffraction however indicated no change in the position of the reflections for $LiMoN_2$, thus confirming the presence of an active phase which is not seen by XRD.

Lithium nitride was seen as a possible source of the impurity due to the presence of lithium in excess during the formation of the nitride. Ammonia synthesis reactions, under both 25% N_2/H_2 and 25% Ar/H_2, were undertaken and the rates of reaction for both feed gases were similar. This led to the conclusion that nitrogen was not required in the feed gas to produce ammonia. The requirement of hydrogen in the feed gas was investigated through a reaction under pure $Ar_{(g)}$. The results were once again comparable to those previously found with the 25% N_2/H_2 and Ar/H_2. This therefore shows that the Li_3N requires no external source of nitrogen or hydrogen in the feed gas to form ammonia. Hence, it can be assumed that the evolution of ammonia is through the direct decomposition of lithium amide.

7 Acknowledgements

8 Supplementary Information

This information can be found on the CD attached to the cover of the thesis.

Information includes:

GSAS refinement data for:

Sample 8 (Li_2MoO_4)

Sample 10 (Li_2MoO_4)

Sample 12 (Li_2MoO_4)

Sample 8 ($LiMoN_2$)

Sample 10 ($LiMoN_2$)

Sample 11 ($LiMoN_2$)

Sample 13 ($LiMoN_2$)

9   References

[1] D. H. Gregory; J. Chem. Soc. Dalton Trans.; (1999) 259

[2] R. Juza, K.Langer and K. von Benda; Angew. Chem., Int. Ed. Eng.; 7 (1968) 360

[3] R. Niewa and F. J. DiSalvo; Chem. Mater.;10 (1998) 2733

[4] C. C. Addison and B. M. Davis; J. Chem. Soc. (A); (1969) 1827

[5] R. Brill; Z. Krystallogr.; 65 (1927) 94

[6] E. Zintl and G. Brauer; Z. Electochem.; 41 (1935) 102

[7] A. Rabenau and H. Schultz; J. Less-common Metals; 50 (1976) 155

[8] B. A. Boukamp and R. A. Huggins; Mater. Res. Bull.; 13 (1978) 23

[9] D. H. Gregory, P. M. O'Meara, A. G. Gordon, D. J. Siddons, A. J. Blake, M. G. Barker, T. A. Hamor and P. P. Edwards; J. Alloys and Comps.; 317 (2001) 237

[10] Z. Stoeva, R. I. Smith and D. H. Gregory; Chem. Mater.; 18 (2006) 313

[11] Z. Stoeva, R. Gomez, D. H. Gregory, G. B. Hix and J. J. Titman; Dalton Trans.; (2004) 3093

[12] D. Fischer and M. Jansen; Angew. Chem. Int. Ed.;41 (2002) 1755

[13] G. V. Vajenine; Inorg. Chem.; 46 (2007) 5146

[14] R. Niewa; Angew Chem. Int. Ed.; 41 (2002) 1701

[15] D. Fischer, Z. Cancarevic, J. C. Schön and M. Jansen; Z. Anorg. Allg. Chem.; 630 (2004) 156

[16] S. J. Clarke, G. R. Kowach and F. J. DiSalvo; Inorg. Chem.; 35 (1996) 7009

[17] S. J. Clarke and F. J. DiSalvo; Inorg. Chem.; 37 (1997) 1143

[18] S. H. Elder, L. H. Doerrer, F. J. DiSalvo, J. B. Parise, D. Guyomard and J. M. Tarascon; Chem. Mater.; 4 (1992) 928

[19] R. Marchand, F. Tessier and F. J. DiSalvo; J. Mater. Chem.; 9 (1999) 297

[20] R. Marchand, Y. Laurent, J. Guyader, P. L'Haridon and P. Verdier; J. Euro. Ceramic Soc.; 8 (1991) 197

[21] N. E. Brese and M. O'Keeffe; Structure and Bonding (Berlin); 79 (1992) 307

[22] H. Zhang, Z. Zhao, C. Xu, A. Duan, W. Lin, H. Tian and I. E. Wachs; Mater. Res. Bull.; 41 (2006) 2334

[23] R. Niewa and H. Jacobs; Chem. Rev.; 96 (1996) 2053

[24] M. Y. Chern and F. J. DiSalvo; J. Solid State Chem.; 88 (1990) 459

[25] U. S. Department of Energy; www.er.doe.gov/sub/accomplishments/decades-discovery/27.html

[26] U. S. Patent No. 5,888,669

[27] F. Tessier, R. Marchand and Y. Laurent; J. Euro. Ceramic Soc.; 17 (1997) 1825

[28] M. G. Barker, M. J. Begley, P. P. Edwards, D. H. Gregory and S. E. Smith; J. Chem. Soc., Dalton Trans.; (1996) 1

[29] D. A. Vennos and F. J. DiSalvo; J. Solid State Chem.; 98 (1992) 318

[30] D. H. Gregory, M. G. Barker, P. P. Edwards and D. J. Siddons; Inorg. Chem.; 34 (1995) 5195

[31] P. S. Herle, M. S. Hedge, N. Y. Vasanthascharya, J. Gopalakrishnan and G. N. Subbanna; J. Solid Sate Chem.; 112 (1994) 208

[32] H. Jacobs and B. Hellmann; J. Alloys and Comps.; 191 (1993)51

[33] P. E. Rauch and F. J. DiSalvo; J. Solid State Chem.; 100 (1992) 160

[34] E. Yeh, N. K. Jaggi, J. B. Butt and L. H. Schwartz; J. Catal.; 91 (1985) 231

[35] E. B. Yeh, L. H. Schwartz and J. B. Butt; J. Catal.; 91 (1985) 241

[36] C. C. Yu, S. Ramanathan and S. T Oyama; J. Catal.; 173 (1998) 1

[37] S. Ramanathan, C. C. Yu and S. T Oyama; J. Catal.; 173 (1998) 10

[38] U. S. Geological Survey;

http://minerals.usgs.gov/minerals/pubs/commodity/nitrogen/nitromcs07.pdf

[39] R. Schlögl; Angew. Chem. Int. Ed.; 42 (2003) 2004

[40] M. R. Hillis, C. Kemball, and M. W. Roberts; Trans. Faraday Soc.; 62 (1966) 3570

[41] K-I. Aika and A. Ozaki; J. Catal.; 14 (1969) 311

[42] L. Volpe and M. Boudart, J. Phys. Chem.; 90 (1986) 4874

[43] R. Kojima and K-I. Aika; Appl. Catal. A; 219 (2001) 141

[44] J. S. J. Hargreaves and D. Mckay; Specialist Periodical Reports in Catalysis, RSC Cambridge; 19 (2006) 84

[45] C. J. H. Jacobsen, S. Dahl, B. S. Clausen, S. Bahn, A. Logadottir and J. K. Nørskov; J. Am. Chem. Soc.; 123 (2001) 8404

[46] D. McKay, D. H. Gregory, J. S. J. Hargreaves, S. M. Hunter and X. Sun; Chem. Comm.; (2007) 3051

[47] C. J. H. Jacobsen; Chem. Comm.; (2000) 1057

[48] J. S. J. Hargreaves and D. McKay; Catalysis; 19 (2006) 84

[49] P. Mars and D. W. van Krevelen; Chem. Eng. Sci. spec. Suppl.; 41 (1954) 263

[50] M, Olea, M. Florea, I. Sack, R. Prada Silvy, E. M. Gaigneaux, G. B. Marin and P. Grange; J. Catal.; 232 (2005) 152

[51] T. W. S. Yip; Personal Communication; 2007

[52] M. Inagaki, Y. Nishikawa and M. Sakai; J. Euro. Ceramic Soc.; 10 (1992) 123

[53] H. M. Reitveld; Acta. Cryst.; 22 (1967) 151

[54] H. M. Reitveld; J. Appl. Cryst.; 2 (1969) 65

[55] A.C. Larson and R.B. Von Dreele; Generalized Structure Analysis System, MS-H805, Los Alamos, NM 87545 (1990)

[56] B. H. Toby; J. Appl. Crystallogr.; 34 (2001) 210

[57] S. Brunauer, P. H. Emmett and E. Teller; J. Am. Chem. Soc.; 60 (1938) 309

[58] U. Kolitsch; Z. Kristallogr.; 216 (2001) 449

[59] A. V. Barinova, R. K. Rastsvetaeva, Yu. V. Nekrasov and D. Yu. Pushcharovskii; Doklady Chem.; 376 (2001) 16

[60] W. H. Zachariasen and H. A. Plettinger; Acta Cryst.; 14 (1961) 229

[61] Natl. Bur. Stand. (US) Monogr.; 25 (1962) 23

[62] L. Volpe and M. Boudart; J. S. S. Chem.; 59 (1985) 332

[63] Z-H. Zhong and K-I. Aika; J Catal; 173 (1998) 535

[64] G. W. Haddix, D. H. Jones, J. A Reimer and A. T. Bell; J. Catal.; 112 (1988) 556

[65] Z. Wei, Q, Xin, P. Grange and B. Delmon; J. Catal.; 168 (1997) 176

[66] R. Kojima and K-I Aika; Appl. Catal. A; 219 (2001) 149

[67] Y. H. Hu and E. Ruckenstein; J. Phys. Chem. A; 107 (2003) 9737